A ratchet-like apical constriction drives cell ingression during the mouse gastrulation EMT

Alexandre Francou, Kathryn V. Anderson[#], Anna-Katerina Hadjantonakis*

Developmental Biology Program, Sloan Kettering Institute, Memorial Sloan Kettering Cancer Center, New York, NY 10065, USA

*Correspondence: hadj@mskcc.org

[#]Deceased

ABSTRACT

Epithelial-to-Mesenchymal Transition (EMT) is a fundamental process in which epithelial cells acquire mesenchymal phenotypes and the ability to migrate. EMT is the hallmark of gastrulation, an evolutionarily conserved developmental process. In mammals, epiblast cells lose pluripotency and ingress at the primitive streak to form mesoderm. Cell exit from the epiblast epithelial layer and the associated EMT are dynamically regulated processes involving a stereotypical sequence of cell behaviors. 3D time-lapse imaging of gastrulating mouse embryos combined with cell and tissue scale data analyses revealed the stochastic-like ingression of epiblast cells at the primitive streak. Ingressing cells constrict their apical surfaces in a pulsed ratchet-like fashion through asynchronous shrinkage of apical junctions. A quantitative analyses of the distribution of apical proteins, revealed the anisotropic and complementary distribution of members of the actomyosin network and Crumbs2 complexes, potential regulators of asynchronous shrinkage of cell junctions. The analysis of mutants demonstrated a requirement for Crumbs2 in Myosin2 localization and activity at apical junctions, and as a candidate for regulating actomyosin anisotropy.

INTRODUCTION

Epithelial-to-Mesenchymal Transitions (EMTs) are morphogenetic programs necessary for the formation of tissues throughout embryonic development, cancer progression and metastasis (Francou and Anderson, 2020; Thiery, 2002; Thiery et al., 2009; Ye and Weinberg, 2015). The EMT that occurs during embryo gastrulation is an evolutionarily conserved event occurring in triploblasts as they form three definitive germ layers (Lim and Thiery, 2012; Nakaya and Sheng, 2008; Thiery et al., 2009).

In amniotes the onset of gastrulation involves formation of the primitive streak at the posterior epiblast, at around embryonic **(E)** 6.5 day in the mouse (Ferrer-Vaquer et al.,

2010; Nakaya and Sheng, 2008; Williams et al., 2012) (Figure 1A). Primitive streak initiation is regulated by the convergence of WNT, BMP and Nodal signals, which together with an FGF input trigger the EMT process (Ferrer-Vaquer et al., 2010; Morgani and Hadjantonakis, 2020; Ramkumar and Anderson, 2011). The basement membrane is broken down at the primitive streak facilitating movement of cells out of the epiblast tissue layer, accompanied by changes in their cell shape, including apical constriction and basal translocation of cell bodies (Ramkumar et al., 2016; Williams et al., 2012). Basal cell ingression and migration away from the epiblast epithelium is facilitated though the dissolution of apical junctions. As cells at the primitive streak undergo EMT, more laterally positioned epiblast cells converge toward the midline (Williams et al., 2012), replenishing the pool for continued ingression and ensuring epithelial integrity.

Apical constriction is an epithelial cell shape change associated with morphogenetic processes such as tissue bending, cell delamination and internalization (An et al., 2017; Chung et al., 2017; Lecuit and Lenne, 2007; Martin and Goldstein, 2014; Nishimura et al., 2012; Samarage et al., 2015; Simoes et al., 2017). The dynamics of apical constriction at gastrulation have been studied in invertebrates, particularly in Drosophila, and shown to be controlled by apical actomyosin contractility (Marston et al., 2016; Martin and Goldstein, 2014; Martin et al., 2009; Mason et al., 2013; Roh-Johnson et al., 2012). Apical constriction has been associated with cell ingression during the gastrulation EMT in chick and mouse (Rozbicki et al., 2015; Serrano Najera and Weijer, 2020; Williams et al., 2012), but how cells dynamically constrict apical surfaces during EMT, and what regulates this process remain open questions. Gastrulation process in Drosophila and mouse cannot be directly compared as they exhibit major different time-scales (20min vs. >24hr days), mechanisms and spatial parameters (tissue invagination vs. cell ingression). In the chick embryo, Myosin-2 plays a role in the formation of the primitive streak and cell ingression from the epiblast layer (Chuai et al., 2006; Rozbicki et al., 2015; Serrano Najera and Weijer, 2020; Voiculescu et al., 2007; Voiculescu et al., 2014). Crumbs2, a protein shown to regulate apical polarity in epithelia, is critical for cell ingression during gastrulation EMT in mouse embryos (Ramkumar et al., 2016). Apical Crumbs2 and Myosin-2B show an anisotropic accumulation in mouse epiblast cells in the vicinity of the primitive streak

(Ramkumar et al., 2016), reminiscent of patterns controlling apical constriction during Drosophila salivary gland development (Roper, 2012), suggesting these proteins are potential regulators of apical constriction during mouse EMT. Visualizing the cellular dynamics of the epiblast during mouse gastrulation has been a longstanding challenge due to its internal location which limits optical access and visualization at high resolution.

Using live imaging of *ex utero* cultured mouse embryos, and high resolution visualization and segmentation of epiblast cell membranes, we performed a dynamic quantitative analysis of apical constriction associated with ingression during the mouse gastrulation EMT. We observed cells undergoing EMT at the mouse primitive streak in a stochastic-like manner, constricting their apical surfaces in a rachet-like pulsed fashion through asynchronous shrinkage of apical cell-cell junctions. By analyzing and quantifying the distribution of apical proteins, we uncovered the anisotropic and complementary distribution of actomyosin network and Crumbs complex proteins consistent with a role in regulating junctional shrinkage and apical constriction. The localization of the apical actomyosin network, as well as two kinases aPKC and Rock1, was perturbed in *Crumbs2* mutants, thereby identifying key components of a putative regulatory network driving apical constriction.

RESULTS

Epiblast cells undergo apical constriction and isolated ingression at the mouse primitive streak

The mouse gastrulation EMT occurs at the primitive streak, which, by contrast to the chick, does not form a morphologically distinct domain (Figure 1A,B). Columnar epithelial epiblast cells with their apical surfaces facing the inner (amniotic) cavity of the embryo apically constrict and elongate basally as they ingress out of the epiblast layer (Figure 1A,C) (Williams et al., 2012). To visualize the dynamic changes in the shapes of all cells in tissue context at single cell during the gastrulation EMT, we sought to label the

103 membranes of all epiblast cells and perform time-lapse imaging. Time-lapse imaging of
104 the epiblast cells in the vicinity of the primitive streak of developing mouse embryos is
105 challenging for several reasons. Embryos need to be kept intact as tissues cannot be
106 microdissected, the epiblast tissue is cup-shaped with inherent curvature and located
107 within the deepest extremity of the embryo (up to 60µm away from the objective), needing
108 to be imaged through the visceral endoderm and mesoderm tissue layers (Figure 1C).
109 Even light-sheet systems, which by merging multi-view data can provide *in toto*
110 visualization of cells in developing embryos, have predominantly been used with nuclear-
111 localized reporters or scattered membrane-labelled cells, data which are less challenging
112 to segment than widespread membrane-localized reporters (McDole et al., 2018).
113
114 We used a ZO-1-GFP protein fusion reporter (Foote et al., 2013) to visualize the tight
115 junction and the apical surface of epiblast cells in order to quantify apical surface
116 dynamics (Figure 1D); and a membrane-localized *R26*$^{mT/mG}$ reporter to visualize their
117 entire plasma membrane and identify completion of apical constriction associated with
118 cell ingression out of the epithelial layer (Figure 1-figure supplement 1A and Video S1).
119 3D time-lapse imaging of embryos at mid/late-streak stage (E7.5) was performed to
120 image the primitive streak) (Figure 1A, B). Time-lapse imaging of ZO-1-GFP embryos
121 revealed that epiblast cells undergo extensive rearrangements as cells on the left and
122 right sides of the embryo converge towards the primitive streak (Figure 1D, Figure 1-
123 figure supplement 1C, Video S2,3) (Williams et al., 2012). The majority of epiblast cells
124 underwent apical constriction and ingression within a ~40µm region in the posterior
125 midline (Figure 1D,E, Video S2), corresponding to the domain of Snail expression and
126 basement membrane breakdown within the epiblast (Francou and Anderson, 2020;
127 Ramkumar et al., 2016; Williams et al., 2012), which by convention defines the primitive
128 streak (Figure 1E dotted lines). Rare apical constriction and ingression events were also
129 observed outside the domain of the primitive streak (Figure 1-figure supplement 1B and
130 Video S3 bottom).
131
132 Within a one hour period 44±2% of cells within the primitive streak domain, constricted
133 and ingressed (mean±s.e.m., n=378 cells, 3 embryos) (Figure 1D,E,F, Video S2), with

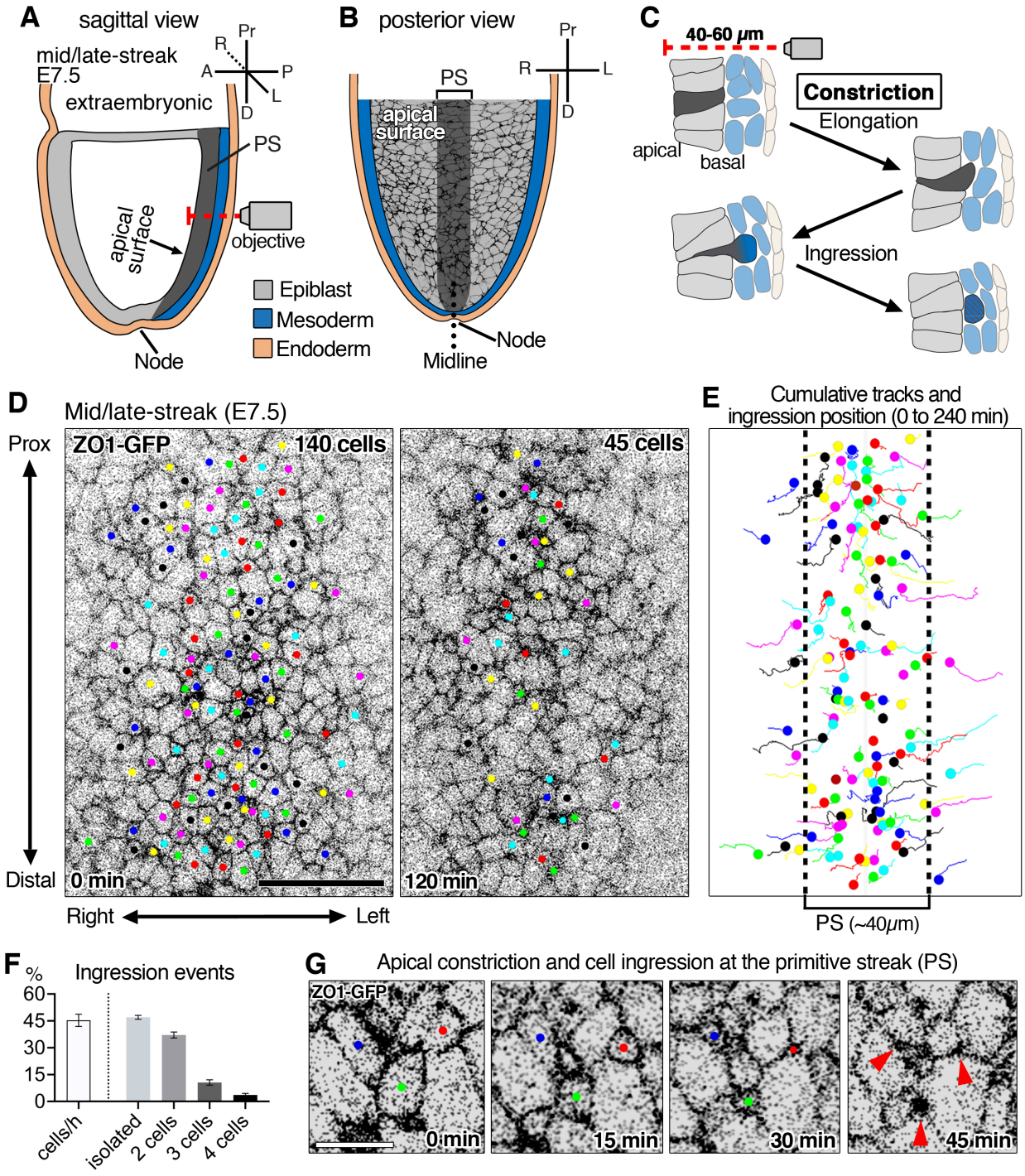

Figure 1: Time-lapse imaging of ZO-1-GFP reporter reveals EMT events at the primitive streak of the mouse gastrula and apical constriction associated with cell ingression. **(A)** Schematic sagittal section view of E7.5 mouse embryo and 3D time-lapse imaging performed from the posterior side with an objective positioned adjacent to the primitive streak (PS). Several tissue layers need to be imaged across (including visceral endoderm and mesoderm) to reach the epiblast apical surface situated furthest from the objective (red dashed line shows the microscope light path). **(B)** Schematic of a view of the epiblast layer apical surface from the

142 inner cavity. The midline (dotted line axis) separates the right and left sides of the embryo. **(C)**
143 High magnification schematic of a sagittal view of an EMT event at the primitive streak depicting
144 a cell constricting its apical surface, elongating basally (dark grey), and ingressing out of the
145 epiblast layer to integrate the mesoderm (blue). Note the apical surface of epiblast cells is
146 located 40-60μm away from the microscope objective. **(D)** Single time-points at t=0min and
147 t=120min of a time-lapse of a ZO-1-GFP embryo. Movies were analyzed as maximum
148 projections of z-stacks to visualize the apical surfaces of cells. Here all the cells that can be
149 followed and observed ingressing during 4hr were tracked. Of 140 cells initially tracked, 95 cells
150 constricted and ingressed over the course of 120min (45 tracked cells remaining). (Time lapse
151 with 5min time interval, 290 cells in the field of view, 140 ingressing cells tracked). **(E)**
152 Cumulative tracking of the 140 cells showing cell tracks over time (lines) and cell position during
153 ingression event (dots). Epiblast cells converge toward the primitive streak (~40μm, dotted
154 lines) where the majority of ingression events occur. **(F)** Graphs showing 44±2.1% of cells in the
155 primitive streak ingress each hour, with 48±1.1% ingressing as single cells, 37±1.7% as pairs of
156 cells, 11±1.5% as triplets (groups of 3 cells), and 4% as groups of 4 cells (of a total of 378
157 ingressing cells analyzed in 3 embryos). **(G)** High magnification view showing the apical
158 constriction of 3 cells at the primitive streak.
159 Pr: proximal, D: distal, A: anterior, P: posterior, R: right, L: left, Ext Emb: extra embryonic region,
160 PS: primitive streak. Error bars represent s.e.m. Scale bars, d, 40μm; g, 10μm.
161 **Figure supplement 1**: Apical constriction and ingression of epiblast cells in the vicinity of the
162 mouse primitive streak.
163
164
165 ingression events appearing to occur stochastically (3-4h). Among the ingressing cells
166 tracked, 48% constricted and ingressed as isolated events (more than 30min apart from
167 adjacent neighboring cells), while the remaining 52% ingressed as pairs, and occasionally
168 as groups of 3-4 cells (less than 30min apart from adjacent neighboring cells) (Figure 1F).
169 At the tissue level the epiblast underwent extensive rearrangement, with some cells
170 moving and acquiring new neighbors prior to their coordinate ingression (Figure 1-figure
171 supplement 1D,E), while others, which were initially neighbors, ingressed at different
172 times (more than 30 min apart) (Figure 1-figure supplement 1D,F).
173
174 **Epiblast cells undergo a ratchet-like pulsed apical constriction during ingression**
175 We next focused on changes associated with the apical surfaces of cells during their
176 ingression. Apical constriction has been extensively studied in Drosophila, including
177 during mesoderm formation and neuroblast delamination (An et al., 2017; Martin et al.,
178 2009; Mason et al., 2013; Simoes et al., 2017), but few studies have investigated the

179 gastrulation EMT in an amniote, and it is unknown how cells constrict their apical surfaces
180 during single cell ingression in the mouse embryo versus the more global constriction and
181 invagination happening during Drosophila gastrulation. To follow changes in apical
182 surfaces during cell ingression, cell membranes were segmented using Tissue Analyzer
183 software (Aigouy et al., 2010; Aigouy et al., 2016) on projections of z-stacks from time-
184 lapse data. By visualizing cells at the primitive streak, we identified apical constriction
185 associated with cell ingression and quantified several parameters, including apical
186 surface area, apical cell surface elongation and orientation, and number of apical
187 junctions (Figure 1G, Figure 2,3-figure supplement 1, Video S4,5). Epiblast cells exhibited
188 a variety of apical surface sizes and shapes that fluctuated over time as they flowed
189 toward the primitive streak. As they initiated apical constriction at the primitive streak,
190 cells exhibited 20-80μm^2 apical surface area, and completed ingression within 25-90min
191 (Figure 2A and Figure 2,3-figure supplement 1B). With the time-scale we are to image
192 and keep living embryos and fluorescent signal integrity, majority of ingressing cells
193 exhibited pulsed constrictions, generally consisting of 2-4 major phases of contraction
194 (Figure 2B,C and Figure 2,3-figure supplement 1F). As cells progressed towards
195 ingression, their number of apical junctions decreased (Figure 2,3-figure supplement 1J,
196 Video S5).
197
198 A closer examination of individual cells allowed us to quantify features of apical surface
199 area throughout the constriction period. The example in Figure 2D depicts the apical
200 surface area of a cell exhibiting 3 main pulses of constriction each separated by more
201 stable intermediate steps (Figure 2C,D, Video S6). While cells showed an average rate
202 of constriction of 1.1±0.1 μm^2/min (mean±s.e.m., n=51 cells, 4 embryos), they exhibited
203 constriction pulses with higher rates of contraction (up to 4.6 μm^2/min), and an average
204 pulse magnitude of 1.4±0.1 μm^2/min (Figure 2B,C,E and Figure 2,3-figure supplement
205 1G). Cells at the primitive streak fluctuated between expansion and contraction before
206 ingression, as did epiblast cells located some distance from the streak (Figure 2C and
207 Figure 2,3-figure supplement 1B,E). During ingression, cells spent 90% of the time
208 contracting apical surfaces (compare with 48% and 55% for epiblast cells away from the
209 streak and before ingression) with an average rate of contraction of 1.1μm^2/min, higher

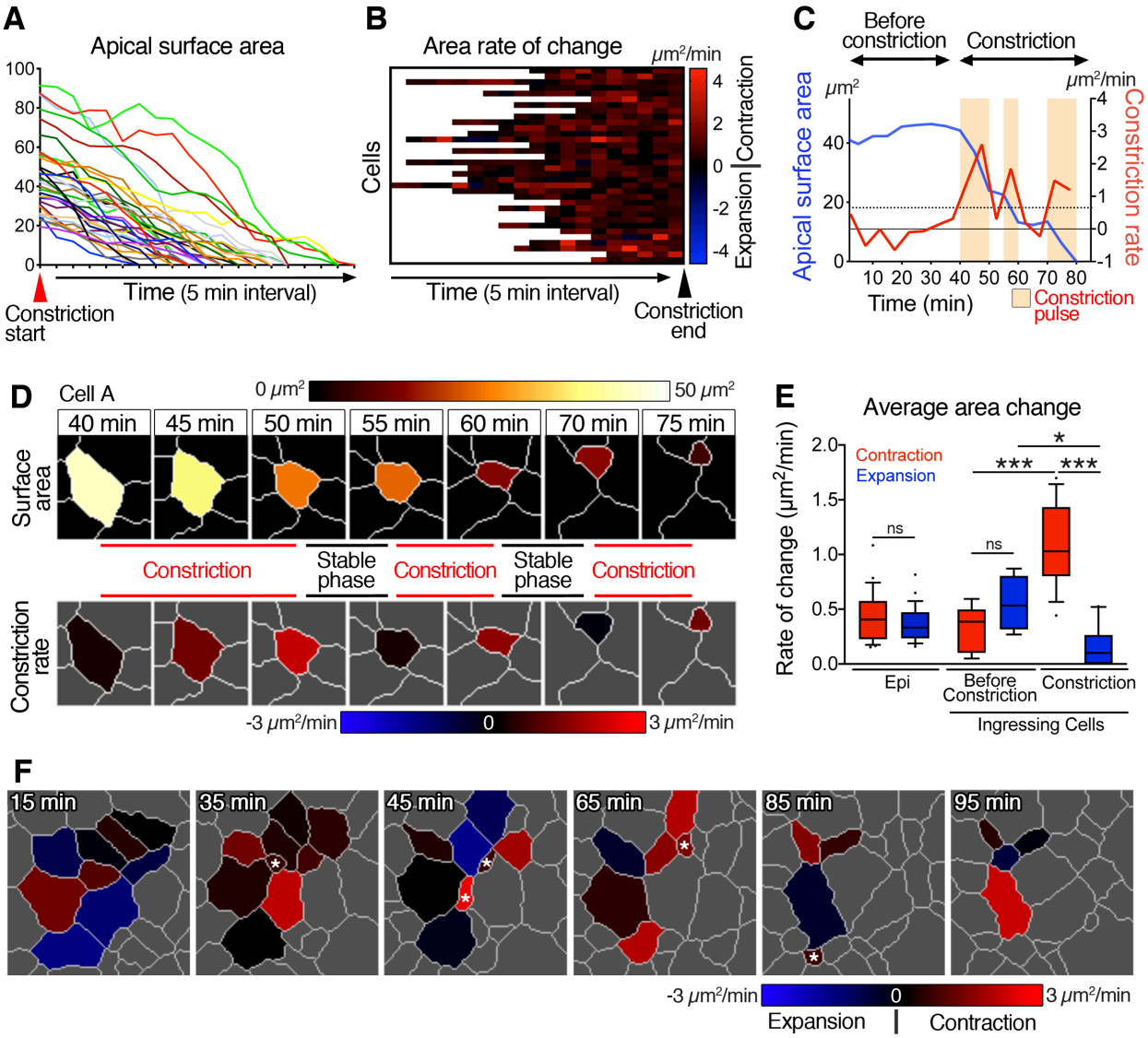

Figure 2: Pulsed racket-like apical constriction during epiblast cell ingression and asynchronous constriction at multi-cellular level. **(A)** Graph showing the apical surface area of a few cells during constriction associated with ingression, aligned to the start of constriction. **(B)** Heat map plot showing the rate of changes of apical surface area of cells during the final constriction period, revealing minimal expansion and pulsed contractions. Each row represents data for an individual cell and are aligned to the end of constriction. **(C)** Graph of apical surface area and rate of constriction of a single cell (cell A) showing slight oscillation in apical surface before undergoing a final constriction period with pulses of constriction, here with three main pulses (beige regions). **(D)** Membrane segmentation and color-coded time-series of apical surface area and constriction rate of a single cell (cell A) showing three pulses of constriction separated by stable steps. (cell corresponding to the plot showed in C). **(E)** Plot showing the average rate of area changes. Epiblast cells away from the primitive streak before ingression show low and equivalent levels of contraction and expansion. Cells at the primitive streak show no significant differences between contraction and expansion before the constriction, whereas rate of

contraction is significantly higher, and expansion reduces during the subsequent constriction period. **(F)** Color-coded time-series and heat map plot of rate of change of apical surface area showing asynchronous oscillation in area and asynchronous constriction and ingression among neighbors. Asterisks show ingression events.
41 cells quantified from 4 embryos. Error bars represent s.e.m. *P<0.05, ***P<0.001 (Unpaired bilateral Mann-Whitney test).
Figure supplement 1: Details and features of constriction pulses and cell parameters during constriction.
Figure supplement 2: Asynchronous apical constriction at the multi-cellular level.

than the average expansion rate of 0.1μm^2/min (Figure 2E and Figure 2,3-figure supplement 1D). To conclude, epiblast cells exhibited fluctuations in apical surface areas before ingression, and pulsed constrictions during ingression at the primitive streak. No hallmark or significant trend was observed at the onset of constriction, the elongation and orientation of the apical surface at the beginning or throughout the constriction period, nor the number of edges when constriction initiated (Figure 2,3-figure supplement 1J-L).

Asynchronous apical constriction at multi-cellular level

We analyzed clusters of cells at the primitive streak to uncover details of the apical constriction behavior at the multi-cellular level. Segmenting cell clusters allowed tracking of cells and documentation of changes in their apical surfaces through time, as cells ingressed (Figure 2F, Figure 2-figure supplement 2, Video S7). Cells underwent fluctuations in apical surface area as some cells constricted and ingressed (Figure 2-figure supplement 2B, Video S7). By color-coding and plotting the rate of apical change, we observed asynchronous oscillation of expansion and contraction phases among neighboring cells. As cells constricted and ingressed, the neighbors did not always exhibit the same behavior; some contracted at the same time, while others slightly expanded or maintained a constant surface area (Figure 2F, asterisk show ingression; S3C and Video S7). Thus, neighboring epiblast cells undergoing EMT and ingressing at the primitive streak displayed asynchronous apical behaviors and ingress in a stochastic-like manner, with some neighboring cells ingressing 2 hours apart, in comparison to Drosophila gastrulation where all ventral furrow cells constrict in less than 10min.

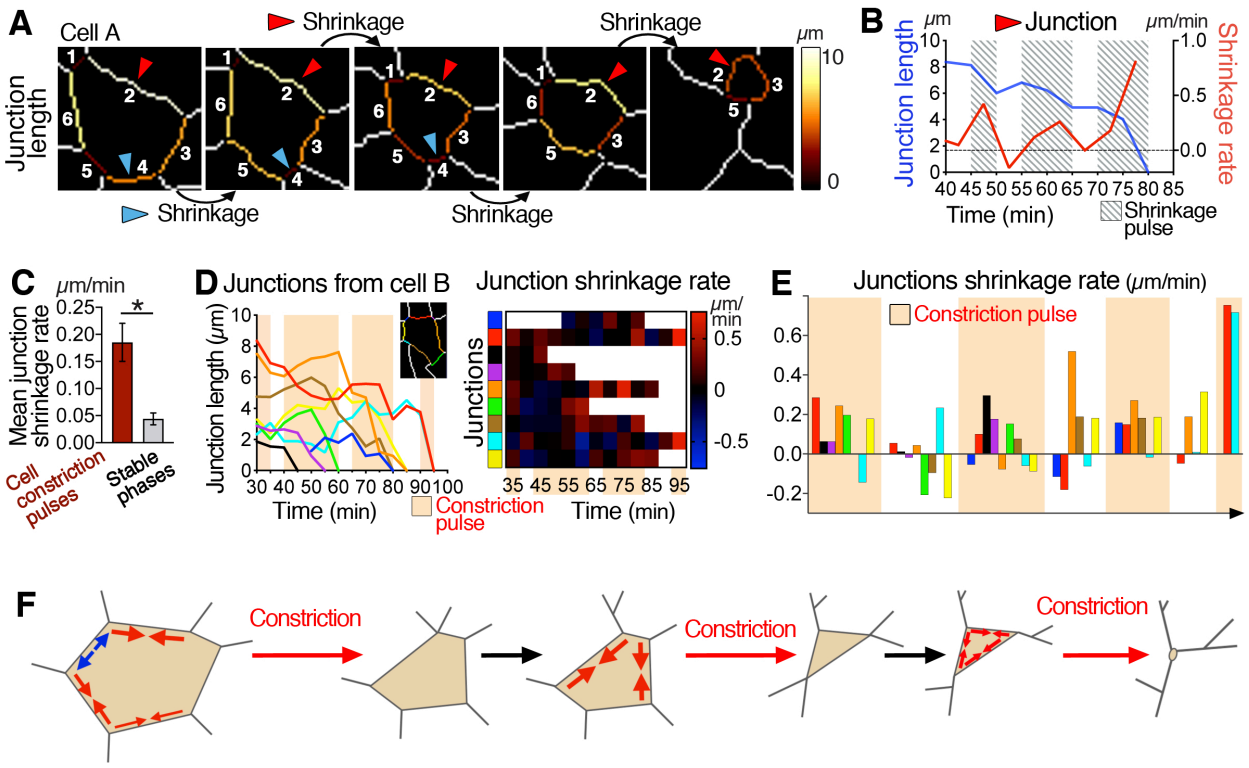

Figure 3: Asynchronous junctional shrinkage during apical constriction. **(A)** Membrane segmentation and color-coded time-series of single junction showing reduction of junctions length during apical constriction of cell A showed in Figure 2. Here the six initial junctions are numbered, and two are pointed (arrowheads) and shrink at different time. **(B)** Graph showing the length and rate of shrinkage of the junction identified with the red arrowhead in A, indicating the 3 main pulses of shrinkage (hatched regions). **(C)** Graph showing increased rate of junctional shrinkage during cell constriction pulses compare to stable phases between constriction pulses from multiple cells (3 embryos, 51 junctions). **(D)** Graph showing the length of individual junctions (left) during apical constriction of a single cell (cell B plotted in Figure 2,3-figure supplement 1A). Junctions reduce their length differentially during the constriction pulses (beige regions). Heat map plot of the shrinkage rate of junctions (right), showing junctions shrinking asynchronously during the constriction pulses (beige time points). Each row represents data for an individual junction, junctions are color-coded as corresponding in the left plot and ordered as neighboring junctions. **(E)** Plot of the average shrinkage rate of each junction through time during each constriction pulse and stables phases, showing the asynchronous shrinkage of different sets of junctions with variable magnitude during the different cell constriction pulses. Junctions are color-coded as neighbors as in D. **(F)** Model of rachet-like pulsed constriction associated with asynchronous junctional shrinkage.

Error bars represent s.e.m. *P<0.05 (Unpaired bilateral Mann-Whitney test).

282

283 **Asynchronous shrinkage of junctions correlates with apical constriction during**
284 **cell ingression**

285 Most apical junctions of any given cell decreased in length in a pulsed manner, with 1-3
286 pulses of shrinkage (Figure 3A,B), with junctions appearing to shrink asynchronously
287 (Figure 3A,D, Video S6). By analyzing and quantifying the behavior of each junction of
288 any one cell during constriction, we noted that the average rate of shrinkage was
289 significantly higher during cell constriction pulses (Figure 3C). Junctions of individual cells
290 shrunk asynchronously (Figure 3D and Figure 2,3-figure supplement 1H,I), differentially
291 and with different magnitudes between one constriction pulse and the next (Figure 3E
292 and Figure 2,3-figure supplement 1H,I), suggesting that asynchronous differential
293 junctional shrinkage may trigger constriction of the cell surface. In sum, epiblast cells at
294 the mouse primitive streak constricted their apical surfaces in a ratchet-like manner, with
295 asynchronous shrinkage of junctions (Figure 3F).

296

297

298 **Anisotropic accumulation of components at apical junctions of epiblast cells**

299 We sought to analyze the localization of apical proteins implicated in epithelial apical
300 constriction in different tissues and species, that could potentially be involved in the apical
301 constriction associated with the mouse gastrulation EMT. E7.5 embryos were
302 immunostained and epiblast apical surface imaged in regions proximo-distally middle of
303 the primitive streak (least curved and best for analysis) (Figure 4-figure supplement 1A).
304 Crumbs2 and Myosin2B have been described as exhibiting heterogenous and
305 complementary distributions at the apical junctions of epiblast cells (Ramkumar et al.,
306 2016), and our data showed Myosin2B and Crumbs2 were predominantly anisotropically
307 distributed, with Crumbs2 exhibited a stronger anisotropy being almost absent from some
308 junctions, and Myosin2B observed on all junctions but at varying levels (Figure 4B and
309 Figure 4-figure supplement 1B).

310

311 We next investigated the localization of other apical proteins, including the actomyosin
312 components, mono- and di-phosphorylated Myosin Light Chain (pMLC and ppMLC),

313 Rock1, a Rho-associated kinase that phosphorylates and activates myosin light chain,
314 and F-actin. We analyzed the localization of the Crumbs complex proteins PatJ, and
315 aPKC, a regulator of non-muscle Myosin2 contexts (Biehler et al., 2021; Petrov et al.,
316 2017; Roper, 2012; Sidor et al., 2020). Membrane segmentation allowed us to
317 systematically quantify several parameters, including apical surface area, cell elongation,
318 and the intensity of junctional protein accumulation (Figure 4A, Figure 4-figure
319 supplement 1C). Two parameters were calculated based on junctional protein intensity
320 and used to evaluate the level of anisotropy: the standard deviation of the junctional
321 intensity measurements cells (SD), and the ratio of the maximum to minimum junctional
322 intensity values (Max/Min) for each cell (Figure 4A). The membrane-GFP reporter served
323 as a control for homogeneous membrane fluorescence localization with low anisotropy
324 and the cohort of proteins analyzed exhibited different degrees of anisotropy (Figure 4B,C
325 and Figure 4-figure supplement 1D,E) . Some proteins such as Crumbs2, ppMLC,
326 ROCK1 and ZO-1 showed a high level of anisotropy (Figure 4B,C and Figure 4-figure
327 supplement 1D,E), though each exhibited a distinct pattern. ZO-1 was observed on all
328 junctions, with variable intensity. Crumbs2 was present on some junctions but absent on
329 others. ppMLC and ROCK1 also exhibited accumulation on some junctions, but low
330 accumulation on others. Other proteins, including PatJ and F-actin, displayed distinct
331 patterns but intermediate anisotropy. Finally some proteins, such as pMLC, Myosin2B
332 and aPKC showed less anisotropy with lower SD and Max/Min values (Figure 4B,C and
333 Figure 4-figure supplement 1D,E). These data allowed us to classify proteins based on
334 their distribution and level of anisotropy. Staining observed at earlier (E7) and later stages
335 (E8) did not show visible differences (data not shown) (Ramkumar et al., 2016).
336
337 The anisotropic membrane accumulation of proteins is relevant with respect to the planar
338 cell polarity (PCP) of epithelial cells. The apical proteins we analyzed did not show a
339 visible planar polarized distribution, which we sought to verify quantitatively.
340
341
342
343

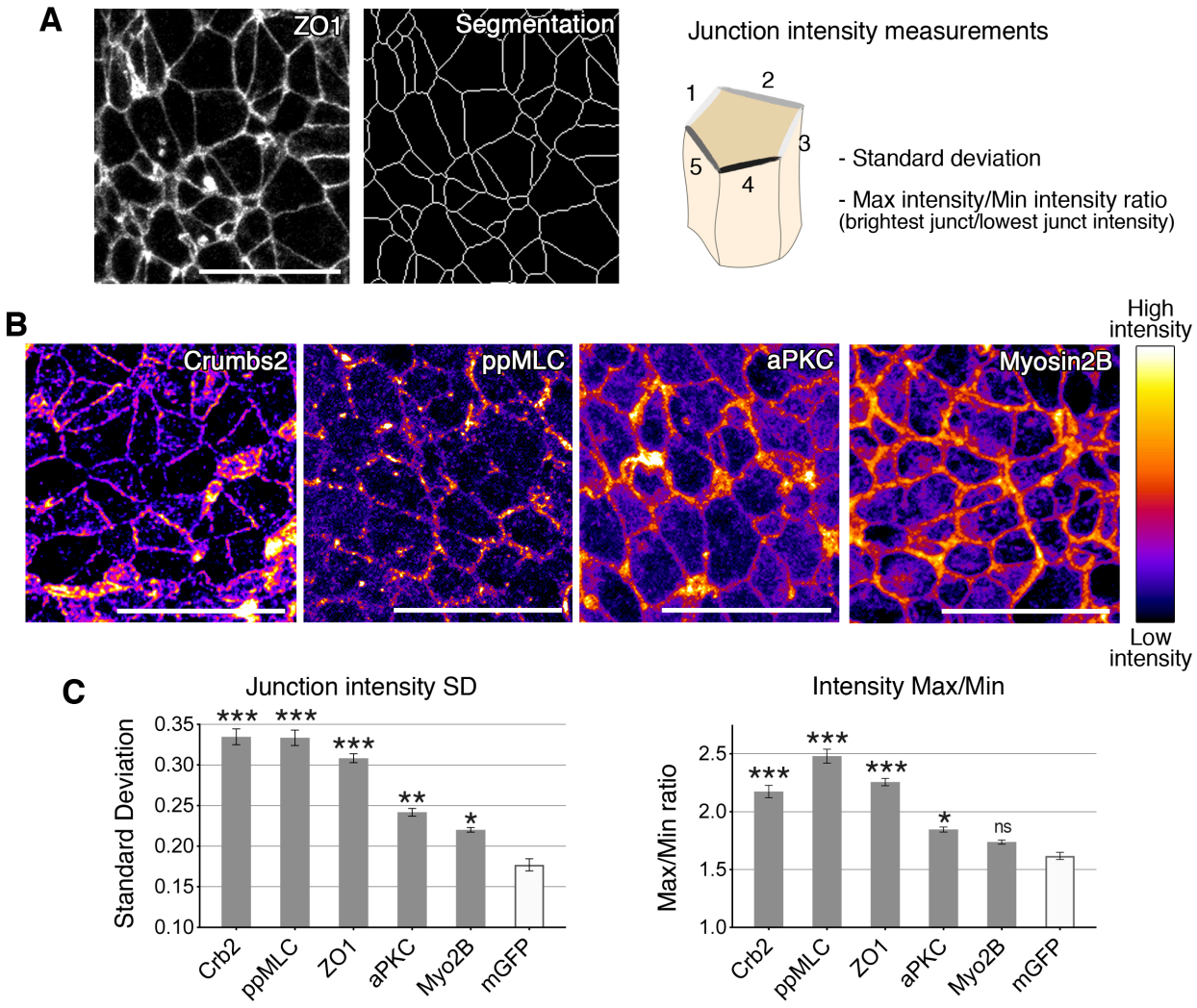

Figure 4: Anisotropic distribution of apical components in epiblast cells at the primitive streak. **(A)** ZO-1 apical membrane localization and corresponding skeleton of membrane segmentation used to quantify junctional intensities and anisotropy parameters as schematized. The average intensities of proteins associated with the junctions of individual cells are used to calculate the standard deviation between junctions, and the difference between junctions with the maximum and minimum intensities. **(B)** Lookup table (LUT) of immunostaining of Crumbs2, di-phosporylated Myosin Light Chain (ppMLC), aPKC and Myosin2B. These proteins show different distributions at apical junctions. Myosin2B and aPKC are present on almost every junction and seem to have a low anisotropy distribution, whereas ppMLC and Crumbs2 are not present on every junction and show a more anisotropic distribution. **(C)** Plots showing the anisotropy parameters, standard deviation and max/min. Proteins such as Crumbs2, ZO-1 and ppMLC show elevated parameters corresponding to a high level of anisotropy, whereas aPKC and Myosin2B show lower anisotropy. The membrane-GFP (recombined mTmG mouse reporter line) is used as control showing homogeneous distribution across all junctions and low anisotropy. (a range of 407-4135 junctions were analyzed in 3-5 embryos for each protein. Statistical test compare each proteins to mGFP).

361 Pr: proximal, D: distal, R: right, L: left, PS: primitive streak. **P<0.01, ***P<0.001 (one-way
362 ANOVA test). Error bars represent s.e.m. Scale bars, 20μm.
363 **Figure supplement 1**: Complementary accumulation of Crumbs2 and Myosin2B, and
364 anisotropy of apical components at the primitive streak.
365 **Figure supplement 2**: Apical proteins show anisotropy accumulation but no planar polarity
366
367
368 We compared the planar polarity index calculated by Tissue Analyzer (amplitude and
369 orientation of polarity) and mean junctional intensity in relation to junction orientation
370 (Figure 4-figure supplement 2) (two ways to assess planar polarity) of apical proteins
371 analyzed to Celsr1, a protein implicated in PCP in mouse and chick (Curtin et al., 2003;
372 Mahaffey et al., 2013; Nishimura et al., 2012). Celsr1 exhibited a planar polarized
373 localization and tended to accumulate on junctions oriented on left-right axis
374 perpendicular to the proximo-distal axis, but by contrast, Myosin2B, Crumbs2, ppMLC,
375 ZO-1 and aPKC, showed no specific axis of planar polarity.
376
377
378 **Reciprocal distribution of apical proteins at apical junctions**
379 We next assessed the colocalization and correlation of the different apical proteins at
380 junctions. Segmentation and intensity values, which served as a readout of concentration,
381 were used to systematically compare mean junctional protein intensities and correlate
382 localization. Some proteins such as ppMLC (di-phosphorylated Myosin Light Chain) and
383 Rock1 showed similar patterns with comparable levels of anisotropy, and appeared to
384 accumulate on the same junctions (Figure 5A). Co-staining revealed a broader
385 accumulation for ppMLC. However, where Rock1 was seen to accumulate, ppMLC was
386 always present, demonstrating strong colocalization (Figure 5A,5C), close to that
387 observed with a positive control staining for ppMLC with two distinct secondary antibodies
388 (Figure 5C and Figure 5-figure supplement 1C,E). F-actin accumulated on most junctions,
389 exhibiting a distinct distribution from ppMLC, whereas F-actin and ppMMLC exhibited a
390 high level of colocalization (Figure 5-figure supplement 1A), with high correlation of
391 junctional intensities (Figure 5C and Figure 5-figure supplement 1A,E). Comparison of F-
392 actin and Rock1 revealed a similar high correlation (Figure 5-figure supplement 1D,E).
393 Thus, the correlated distributions of ppMLC, Rock1 and F-actin proteins suggests they

394 could function at the same junctions. Despite exhibiting anisotropy, ZO-1 and aPKC were
395 observed to be present on all junctions (Figure 4A,B and S3), with a high level of
396 correlation, similar to a positive control (Figure 5-figure supplement 1D,E), demonstrating
397 their accumulation on the same junctions.
398
399 By contrast, when comparing other junctional proteins, we observed very low or no
400 correlation. Crumbs2 and Myosin2B exhibited a complementary localization (Figure 5B),
401 with minimal colocalization. Comparisons of Crumbs2-Myosin2B junctional intensities
402 revealed a broad distribution and very low correlation (Figure 5B,C). Comparing PatJ, a
403 Crumbs partner protein, with pMLC (phosphorylated-Myosin Light Chain) showed a
404 similar accumulation with almost no correlation (Figure 5C and Figure 5-figure
405 supplement 1B,E). Analysis of other protein pairs, including ZO-1-ppMLC, and aPKC-
406 ppMLC revealed low correlation (Figure 5-figure supplement 1D,E).
407
408 To gauge the non-complementarity and assess potential anti-correlation of certain
409 proteins, we analyzed junctional intensity correlations grouped by individual cells, rather
410 than junctions collectively. This analysis confirmed the strong correlation of ppMLC,
411 Rock1 and F-actin, where most cells exhibited a positive correlation trend with a high
412 correlation coefficient (Figure 5-figure supplement 2A,B). For pairs of proteins such as
413 Crumbs2 and Myosin2B, and PatJ and pMLC, which showed no correlation when junction
414 quantifications were compared (Figure 5B,C and Figure 5-figure supplement 1), grouping
415 junction intensities by individual cells revealed a broad distribution; some cells showed
416 anti-correlation, some no correlation and some positive correlation (Figure 5-figure
417 supplement 2C-F). This analysis illustrated a heterogeneity across the epiblast population
418 in the vicinity of the primitive streak, at any one time, supporting our hypothesis that
419 anisotropic accumulation patterns are dynamic.
420
421 These quantitative analyses of apical protein anisotropy patterns combined with the
422 correlation of distributions, allowed us to define two groups of proteins that tend to
423 accumulate on different junctions. Cytoskeletal proteins including Myosin2,
424 phosphorylated MLC, ROCK1 and F-actin predominantly accumulate on the same

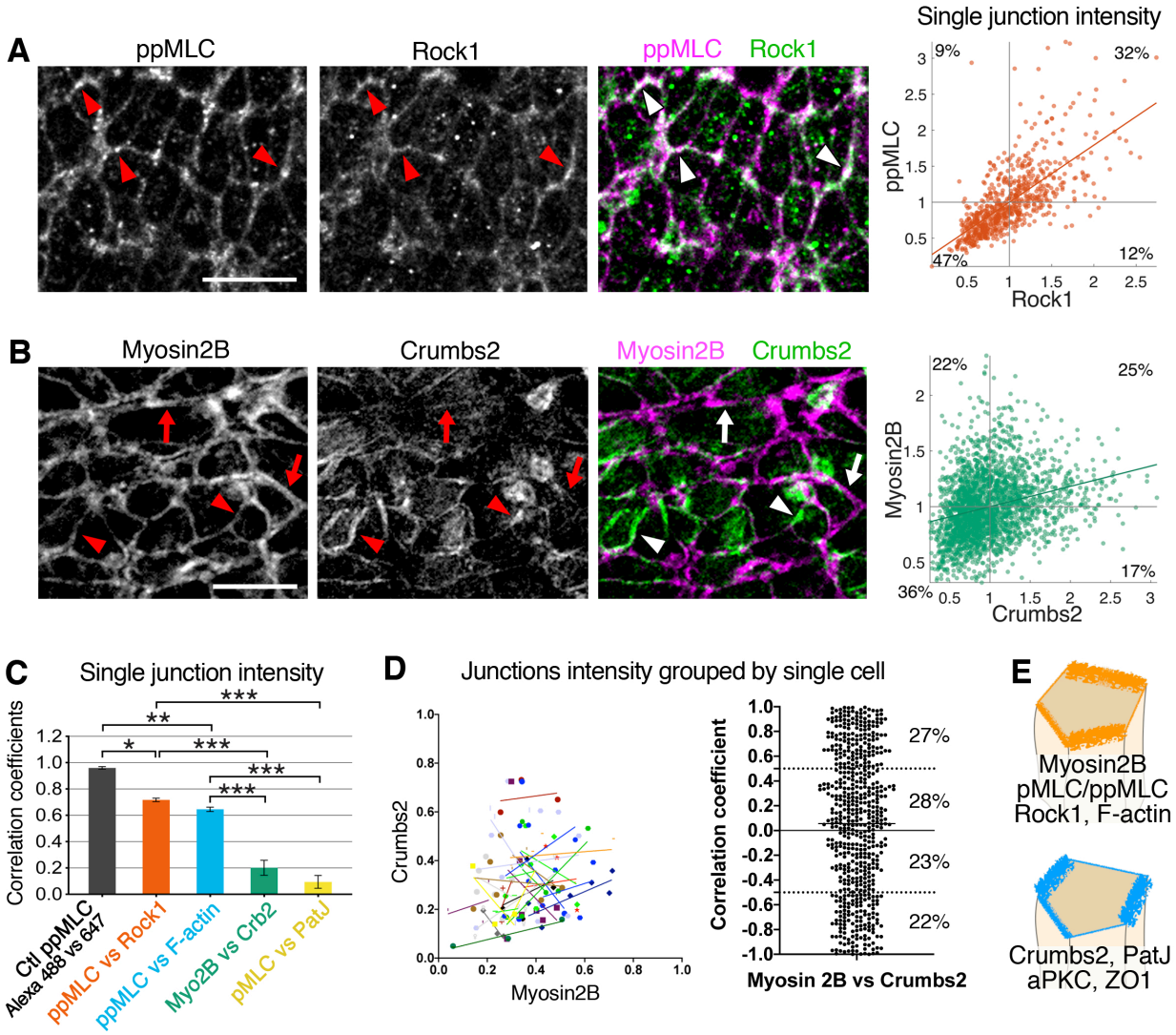

Figure 5: Complementarity accumulation of apical components at apical junctions. **(A)** Co-immunostaining of ppMLC and Rock1 reveals a tendency to accumulate on the same junctions. Note colocalization of fluorescent signal on most junctions (arrowheads). Scatter plot on the right showing elevated intensity correlation of the two proteins. Each point represented the mean intensity at a single junction. **(B)** Co-immunostaining of Myosin2B and Crumbs2 reveals that they tend to accumulate on different junctions. Note junctions where Myosin accumulation predominates (arrows), and junctions where Crumbs2 predominates (arrowheads). Corresponding scatter plot shows a low correlation. **(C)** Plot showing the correlation coefficients associated with the different scatter plots. Proteins such as ppMLC, Rock1 and F-actin exhibit a strong correlation with a high coefficient (ppMLC vs Rock1=0.72±0.01, ppMLC vs F-actin=0.65±0.02), whereas others including Myosin2B and Crumbs2, PatJ and pMLC exhibit much lower correlation with low coefficient (Myosin2B vs Crumbs2=0.20±0.06, pMLC vs

438 PatJ=0.09±0.05). **(D)** Example of scatter plot showing the junctional intensity correlation of
439 Crumbs2 and Myosin2B in a cohort of cells. Each symbol represents one junction, grouped by
440 cells (color coded) with respective correlation trends, depicting a mix of cells with correlation,
441 some with no correlation, and some with anti-correlation. Graph on the right shows correlation
442 coefficients for a larger number of cells, showing a broad distribution, from correlation (+1) to
443 anti-correlation (-1). % show the distribution of correlation coefficients in the different quarters.
444 **(E)** Based on co-staining for multiple apical proteins and measurements of anisotropy and
445 correlation, two groups of proteins can be defined with a tendency to accumulate on same
446 junctions: actomyosin components, and apical determinants and junctional proteins.
447 711-2453 junctions were quantified in 3-4 embryos for each pair of proteins. *P<0.05,
448 ***P<0.001 (one-way ANOVA test). Error bars represent s.e.m. Scale bars, 10μm.
449 **Figure supplement 1**: Correlation of protein distributions at apical junctions.
450 **Figure supplement 2**: Junctional correlation of proteins at the single cell level.
451
452
453 junctions, while apical components and junctional proteins such Crumbs2, PatJ, aPKC,
454 ZO-1 will co-localized on other junctions (Figure 5D). This anisotropic distribution of the
455 actomyosin network and Crumbs-complex associated proteins is associated with
456 dynamic apical constriction.
457
458
459 **Cellular defects in *Crumbs2*$^{-/-}$ mutant embryos at the primitive streak**
460 Crumbs2 is an important regulator of the mouse gastrulation EMT, where it promotes cell
461 ingression. Epiblast cells fail to ingress and accumulate at the primitive streak in *Crb2*$^{-/-}$
462 embryos (Ramkumar et al., 2016). By quantifying the apical surface of posterior epiblast
463 cells at E8.0, we observed increased cell density and cells with smaller apical surfaces
464 around the primitive streak of mutants, as compared to littermate controls (Figure 6,7-
465 figure supplement 1A). This cell crowding was not observed half a day earlier at E7.5
466 (Figure 6,7-figure supplement 1B) (Ramkumar et al., 2016) when mutant embryos were
467 morphologically indistinguishable from wild-type stage-matched counterparts.

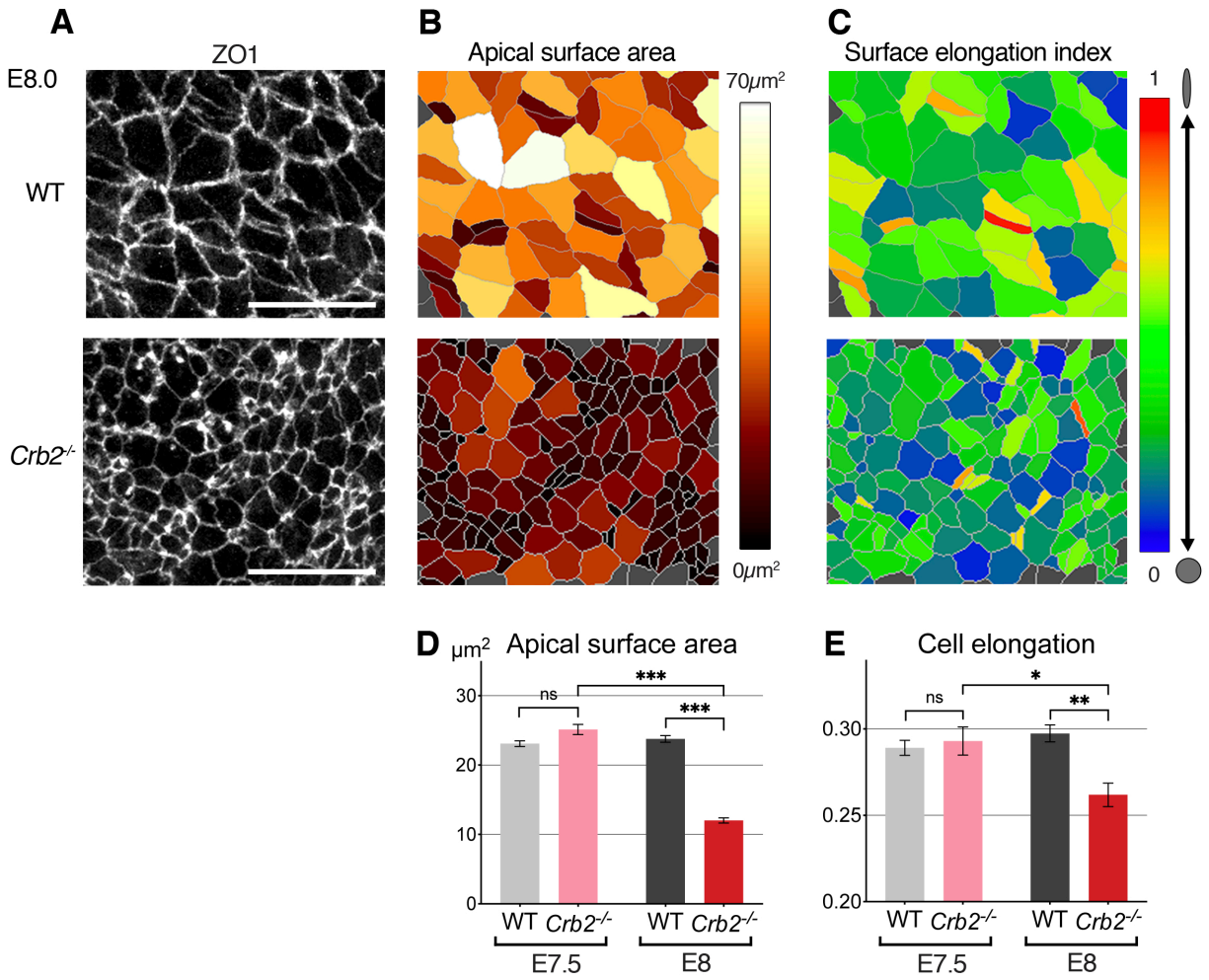

Figure 6: Cellular defects in Crumbs2 mutant embryos at the primitive streak. **(A)** ZO-1 immunostaining showing the apical surface of WT and *Crumbs2* mutant embryos at E7.5 and E8.0. **(B)** Segmentation and color code of apical surface areas reveals smaller surfaces in *Crumbs2* mutants at E8.0. **(C)** Color code of cell surface elongation index calculated by Tissue Analyzer (regardless of their axis) reveals rounder surfaces in *Crumbs2* mutants at E8.0. **(D)** Graph of quantifications showing significantly smaller apical surfaces in *Crumbs2* mutants at E8.0 compared to E7.5, and to WT embryos. **(E)** Graph showing significantly less elongated apical surfaces in *Crumbs2* mutants at E8.0 compared to E7.5, and to WT embryos. 334-1187 cells from 3-5 embryos were quantified for each genotype and stage. ***P<0.001 (Unpaired bilateral Mann-Whitney test). Error bars represent s.e.m. Scale bars, 20μm.

Morphological defects (apical surface areas and surface elongation) in cells at the primitive streak were first detected at E8.0 with cells having smaller and rounder apical surfaces (Figure 6A-E and Figure 6,7-figure supplement 1B) resulting from their failure to ingress, and consequent accumulation in the epiblast.

486

487 **Molecular defects in *Crumbs2*$^{-/-}$ mutant embryos precede cellular defects**

488 To identify molecular defects associated with and preceding the ingression defect we
489 analyzed the distribution of actomyosin components in *Crb2*$^{-/-}$ embryos. Although ZO1
490 distribution appeared unchanged in the mutants, suggesting the integrity of junctions was
491 not altered, we observed reduced levels of Myosin2B and ppMLC (the fully activated form
492 of Myosin Light Chain) in mutants at E7.5 (Figure 7A,B) and Figure 6,7-figure supplement
493 1C). We also observed more diffuse and reduced cortical actin filaments at the apical
494 junctions of epiblast cells in mutants, whereas the medial pool of actin appeared slightly
495 increased (Figure 7A,B). Thus, actomyosin apical accumulation and activity were
496 perturbed without alteration of junctional integrity in *Crb2*$^{-/-}$ embryos at E7.5, preceding
497 morphological defects.

498

499 We next focused on aPKC and Rock1, implicated in the regulation of the actomyosin
500 network by Crumbs in Drosophila and cultured cells (Biehler et al., 2021; Ishiuchi and
501 Takeichi, 2011; Roper, 2012; Sidor et al., 2020). By quantifying the intensity of aPKC and
502 Rock1 at junctions, we observed a 3-fold reduction of aPKC intensity at apical junctions
503 and a more diffuse signal in the cytoplasm, and we observed a slight reduction of
504 junctional Rock1 (Figure 7C and Figure 6,7-figure supplement 1D). These observations
505 suggest a network with aPKC and Rock1 regulating actomyosin downstream of Crumbs2.
506 By quantifying the two parameters used to assess anisotropic distributions at apical
507 junctions, we observed that in *Crb2*$^{-/-}$ embryos the SD and Max/Min of junction intensity
508 of Myosin2, F-actin ZO-1, aPKC and Rock1 was reduced (Figure 7D), revealing reduced
509 anisotropy and more homogenous distribution of these proteins.

510

511

512

513

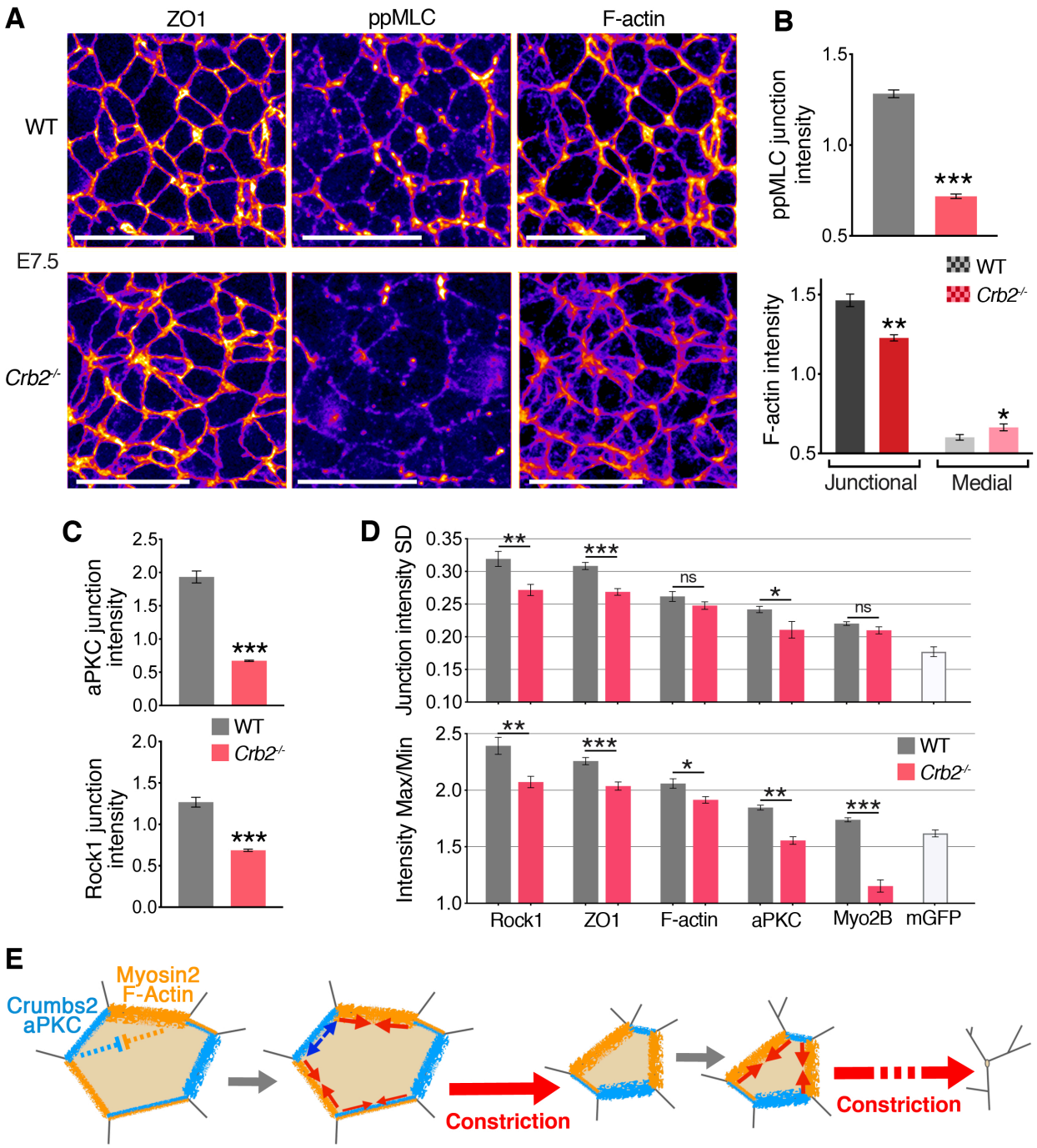

Figure 7: Molecular defects in *Crumbs2* mutants preceding visible cellular defects. **(A)** Co-immunostaining for ZO-1, ppMLC and F-actin in WT and *Crumbs2* mutants at E7.5 reveal reduced ppMLC and F-actin junctional intensities. **(B)** Plots showing intensity measurements of junctional ppMLC and F-actin. ppMLC shows significant decrease in junctional accumulation in *Crumbs2* mutants. F-actin shows lower junctional accumulation and increased diffuse medial intensity in *Crumbs2* mutants. **(C)** Graphs of junctional intensity measurements showing significantly decreased aPKC and Rock1 intensity in *Crumbs2* mutants compared to WT. **(D)** Anisotropy parameters, Standard Deviation and Max/Min showing perturbed junctional

accumulation anisotropy in *Crumbs2* mutants compared to WT embryos. ZO-1, F-actin, Myosin2, aPKC and Rock1 show reduced anisotropy in *Crumbs2* mutants. **(E)** Working model. Actomyosin network and Crumbs2 complex show anisotropic and complementary distribution at apical junctions of epiblast cells at the primitive streak. These distributions are likely dynamic through time and heterogenous among cells, and could potentially regulate each other distribution. Junctions asynchronously shrink and allow ratchet-like constriction of apical surfaces, facilitating cell constriction and ingression without creating increased tension within the tissue.
122-501 cells in 3-4 embryos were quantified for each genotype and proteins. *P<0.05, **<0.01, ***P<0.001 (B,C: Unpaired bilateral Mann-Whitney test; D: one-way ANOVA test). Error bars represent s.e.m. Scale bars, 20μm.
Figure supplement 1: Cellular and molecular defects in *Crumbs2* mutant embryos.

DISCUSSION

To develop a dynamic mechanistic understanding of the mouse gastrulation EMT at cellular resolution and tissue-scale we 3D time-lapse imaged *ex utero* cultured embryos. We used membrane tagged reporters and quantified the spatiotemporal features of apical cell surfaces, junctions and junctional composition of cells in the vicinity of the primitive streak. Our analyses reveal that after converging at the primitive streak, epiblast cells undergo EMT, either individually or in small groups of cells, in what appear to be stochastic events. Cells constrict their apical surfaces in a ratchet-like manner during ingression from the epiblast epithelium. Constriction is associated with the anisotropic apical distribution of actomyosin network and Crumbs2 complex proteins.

Apical constriction is an evolutionarily conserved behavior associated with gastrulation in invertebrates such as Drosophila, nematodes and sea urchins, as well as in vertebrates and amniotes, such as Xenopus and chick (Christodoulou and Skourides, 2015; Lecuit and Lenne, 2007; Martin and Goldstein, 2014; Martin et al., 2009; Rozbicki et al., 2015). We observed fluctuations in the size and shape of the apical surface of epiblast cells as they converged towards the streak. In the vicinity of the streak, and as cells ingressed, their apical surfaces predominantly constricted, in a step-wise ratchet-like manner.

558 Pulsed ratchet-like apical constrictions have been observed in Drosophila gastrulation,
559 where cells at the ventral furrow constrict in a short period of time to drive tissue
560 invagination, followed by en-masse cell delamination (Martin et al., 2009; Mason et al.,
561 2013). Drosophila neuroblast delamination also exhibits a ratchet-like apical constriction
562 (An et al., 2017; Simoes et al., 2017). Despite these similarities, mesoderm formation
563 process during gastrulation of Drosophila and mouse cannot be directly compared as they
564 exhibit different time-scales, mechanisms and spatial parameters. In Drosophila the entire
565 ventral furrow constricts in less than 10min, triggering a tissue-wide invagination without
566 cell ingression, thereafter cells lose their epithelial properties and form a mesenchymal
567 mesodermal tissue. By contrast, in the mouse embryo epiblast cells at the primitive
568 undergo constriction and ingression in a more isolated fashion over the course of almost
569 2 days. Our time-lapse imaging revealed a ratchet-like apical cell constriction operating
570 in the mouse gastrulation EMT, where cells predominantly ingress as isolated cells or
571 small cluster, versus the en-masse constriction and invagination taking place in
572 Drosophila.
573
574 We further demonstrated that this apical constriction is associated with the asynchronous
575 contraction of junctions between neighboring cells, potentially regulated by the apical
576 actomyosin network. During Drosophila gastrulation, an apico-medial network of
577 actomyosin pulls apical cell junctions to simultaneously reduce their length and allow the
578 constriction of apical surface of cells at the ventral furrow (Coravos and Martin, 2016;
579 Martin et al., 2009; Mason et al., 2013). Drosophila neuroblasts exhibit polarized apical
580 constriction driven by both planar polarized junctional and medial actomyosin networks,
581 predominantly leading to a loss of antero-posterior junctions (Simoes et al., 2017). In the
582 mouse gastrula, we found that cells undergoing EMT contract and lose cell-cell junctions
583 in an asynchronous manner without apparent planar polarity. Our analyses of the
584 junctional distribution of Myosin2 supports its potential involvement in regulating
585 constriction during ingression, but does not exclude an additional role played by a medial
586 pool. Pulsed actomyosin activity has been documented in various processes involving
587 cell shape changes, including epithelial apical constriction (Coravos et al., 2017; Heer
588 and Martin, 2017; Martin and Goldstein, 2014). The pulsed constriction we observe in

589 mouse gastrulation indicates conservation of this actomyosin behavior, as a general
590 mechanism that integrates assembly and disassembly of the network and rearrangement
591 and recruitment of Myosin and Actin molecules. Furthermore, pulsed contractility could
592 allow a substantial but transient constriction of epiblast apical surfaces during ingression
593 without creating deleterious tension which could impact the integrity of the tissue.
594
595 Since large numbers of cells undergo EMT and leave the epiblast epithelium at any given
596 time, simultaneous constriction and ingression of multiple neighboring cells could exert
597 extreme tension and deformation in the tissue. Our observation of a stochastic and
598 asynchronous constriction of neighboring cells provides a parsimonious explanation for
599 maintaining epithelial integrity, and a continuation of ingression events at the primitive
600 streak and tail bud for almost 2 days throughout gastrulation, in comparison to Drosophila
601 gastrulation where all ventral furrow cells constrict in less than 10min. Cell division taking
602 place on the basal side of an epiblast layer, has been reported at the primitive streak
603 where it has been proposed to facilitate cell ingression (Mathiah et al., 2020). Apical
604 constriction and basal cell division could therefore work in concert to promote the correct
605 number of cell ingression events.
606
607 Myosin2 is a driver of membrane movement and apical constriction in various contexts
608 (An et al., 2017; Chung et al., 2017; Marston et al., 2016; Martin and Goldstein, 2014;
609 Martin et al., 2009; Mason et al., 2013; Nishimura et al., 2012; Roh-Johnson et al., 2012;
610 Samarage et al., 2015; Simoes et al., 2017). Crumbs2 is involved in the EMT process
611 during mouse gastrulation and exhibits a complementary localization to Myosin2
612 (Ramkumar et al., 2016) (our data). Anisotropic membrane localization of Crumbs has
613 been implicated in Drosophila salivary gland development, where it controls the
614 localization of actomyosin cables at the placode border, necessary for apical constriction
615 and tissue invagination (Roper, 2012). Recently, Crumbs has also been implicated in
616 apical constriction during neuroblast cell ingression in Drosophila (Simoes et al., 2022).
617 We observed the anisotropic and complementary localization of Crumbs2 and Myosin2,
618 and have identified other proteins exhibiting anisotropic distributions. Although Myosin2B,
619 F-actin, aPKC and ZO-1 are present on all apical junctions, they exhibit a differential

620 anisotropic accumulation between the junctions of any one cell. Other proteins such as
621 ppMLC and the myosin kinase Rock1, as well as Crumbs2 and its partner PatJ, exhibited
622 a higher level of anisotropy. In the Drosophila salivary gland placode border, Crumbs and
623 Myosin2 show planar polarized localization with Crumbs being absent from cell junctions
624 that contact the border of the placode, allowing the accumulation of myosin II at the
625 placode border and formation of a supracellular actomyosin cable (Roper, 2012). By
626 contrast, our results in mouse show that Crumbs2, Myosin2B and several other proteins
627 do not exhibit planar polarity, but what appears to be a disordered anisotropy. Our studies
628 reveal a patterned distribution in which actomyosin regulators and Crumbs2, aPKC and
629 ZO-1 accumulate on subsets of cell junctions and display complementary distributions.
630 We propose that these anisotropic patterns are dynamic and control the asynchronous
631 junction contraction associated with apical constriction.
632
633 Crumbs2 acts through aPKC and Rock to regulate Myosin2 localization in the *Drosophila*
634 salivary gland (Roper, 2012), and aPKC has been shown to regulate Myosin2 junctional
635 localization and activity both positively and negatively in different context, directly or
636 through other proteins (Biehler et al., 2021; Ishiuchi and Takeichi, 2011; Petrov et al.,
637 2017). The regulation of Myosin2 by Crumbs and aPKC through Rock in *Drosophila*
638 salivary gland development is complex (Sidor et al., 2020), and despite Rock membrane
639 association being tightly regulated by Crumbs across the tissue, regionally distinct
640 behaviors have been observed. At placode borders, cells exhibit a polarized accumulation
641 of Crumbs/aPKC and Rock to control actomyosin cable formation, whereas in the center,
642 where cells constrict during the tissue invagination, both Crumbs and Rock are
643 isotropically present at junctions (Chung et al., 2017; Sidor et al., 2020). Our results
644 demonstrate that during mouse gastrulation Crumbs2 controls the apical accumulation
645 and activity of actomyosin, which could account for the defects in apical constriction and
646 ingression in Crumbs2 mutants. We observed Crumbs2 as required for the correct
647 accumulation and distribution of aPKC, Myosin2, Rock1 and F-actin at apical junctions,
648 without alteration of junctional integrity. Crumbs2 along with aPKC could control the
649 anisotropic accumulation of actomyosin, triggering asynchronous junctional reduction
650 resulting in apical constriction during ingression (Figure 7E).

651

652 In ingressing mouse epiblast cells Crumbs2 together with aPKC and Rock1 could
653 represent a complex network implicating other proteins, required for Myosin2 localization
654 and activity at the apical membrane, but also potentially regulating the anisotropic
655 accumulation of the actomyosin network locally at junctions, facilitating correct apical
656 constriction during ingression (Figure 7E). Our work reveals that pulsed ratchet-like
657 constriction behaviors observed in different species and distinct contexts are conserved
658 in the mouse gastrulation EMT.

659

660

661

662 **METHODS**

663

664 **Experimental animals**

665 FVB or mixed background mice were used for immunofluorescence staining. Most other
666 experiments, incorporating genetically engineered mouse models, were carried out in a
667 mixed background. The *Gt(ROSA)26Sor*$^{tm4(ACTB\text{-}tdTomato,\text{-}EGFP)Luo}$/J (Muzumdar et al.,
668 2007) (referred to throughout as mT/mG) line was obtained from the Jackson
669 Laboratory and crossed to Sox2-Cre (Hayashi et al., 2002) mice to generate a
670 membrane-GFP reporter. The ZO-1-GFP protein fusion knock-in mouse reporter a gift
671 from Terry Lechler (Duke University Medical Center, NC, USA) (Foote et al., 2013;
672 Huebner et al., 2014). *Crumbs2*$^{+/-}$ animals were generated from animals carrying a
673 conditional allele of Crumbs2 via germline deletion (Alves et al., 2013). Animals were
674 housed and bred in accordance with institutional IACUC guidelines. The MSKCC
675 IACUC approved all experiments.

676

677 **Embryo dissection, immunostaining and antibodies**

678 For the majority of immunostaining experiments, embryonic day E7.5 and E8.0 embryos
679 were dissected in cold PBS and fixed for 1 hour in 4% PFA, with the exception that 8%
680 PFA was used for detection of phosphorylated myosin. Whole-mount embryos were
681 blocked overnight in blocking buffer (PBS; 0,1%Triton; 3%BSA), incubated overnight at

682 4°C with primary antibodies, washed in blocking buffer and incubated overnight at 4°C
683 with species-specific secondary antibodies. For staining of F-actin embryos were
684 incubated with Phalloidin-FITC/TRITC (Invitrogen).
685
686 The following antibodies were used: rabbit anti-Myosin Heavy Chain 2B (1/400, Biolegend
687 909902), mouse anti-Myosin Heavy Chain 2B (1/50, DSHB CMII 23), rabbit anti-pMLC
688 (1/200, Cell Signaling Ser19 3671), mouse anti-pMLC (1/200, Cell Signaling Ser19 3675),
689 rabbit anti-ppMLC (1/200, Cell Signaling Thr18/Ser19 3674), rat anti-ZO-1 (1/50, DSHB
690 R26.4C), mouse anti-ZO-1 (1/200, Invitrogen 33-9100), rabbit anti-ZO-1 (1/200, Zymed
691 61-7300), mouse anti-aPKCλ (1/100, BD bioscience 610207), chick anti-GFP (1/400,
692 Abcam 13970). Rabbit anti-Crumbs2 was a gift from Jane McGlade (Hospital for Sick
693 Children, Toronto, Canada) and was used at 1/50 (Laprise 2006). Rabbit anti-PatJ was a
694 gift from Andre Le Bivic (Developmental Biology Institute of Marseille, France) and was
695 usedc at 1/200 (Lemmers 2002). Rat anti-Rock1 was a gift from Masatoshi Takeichi
696 (RIKEN Center for Developmental Biology, Kobe, Japan) and used at 1/100 (Nishimura
697 and Takeichi 2008). Guinea Pig anti-Celsr1 was a gift from Danelle Devenport (Princeton
698 University, Princeton, USA) and was used at 1/500 (Devenport and Fuchs 2008).
699 Fluorescent secondary antibodies Alexa 488, 568 and 647 from Life Technologies and
700 ThermoFisher were used at 1/500.
701
702 **Fixed embryo epiblast mounting and imaging**
703 Following staining, embryos were microdissected to retain the posterior side containing
704 the primitive streak and mounted on glass slide and coverslipped in Fluoromount-G, with
705 the cavity and apical surface of the epiblast facing the coverslip. Layers of tape were
706 placed on both extremity of the slide to create a slight volume and to avoid extensive
707 compression and flattening of the tissue. The position of the primitive streak was
708 determined to coincide with the posterior midline running from the allantois to the node
709 (two morphologically distinguishable structures), and streak axis was oriented so that the
710 proximo-distal axis was oriented along the vertical axis of the image. Most
711 immunostaining revealed a high concentration of puncta also allowing us to identify the
712 location of the primitive streak after imaging. Embryos were imaged on a Leica SP8 or a

713 Zeiss LSM880 laser point scanning confocal using x40 oil immersion objectives, and
714 images were acquired as Z-stacks with 1µm step.
715
716 **Segmentation and quantification of fixed embryo staining**
717 Confocal images were analyzed using ImageJ. The primitive streak region was located
718 and a maximal intensity projection of a minimal thickness (5-10µm) was generated to
719 observe the apical surface of cells in a selected region of interest at the primitive streak.
720 ZO-1 localization was generally used as an apical junction marker for segmentation.
721
722 Segmentation was performed using the Tissue Analyzer software (Aigouy et al., 2010;
723 Aigouy et al., 2016), an ImageJ plugin which uses a watershed algorithm to segment the
724 cell cortex. Briefly, a first membrane segmentation was automatically performed, and then
725 verified and corrected manually. Cells and junctions were tracked and assigned IDs. Most
726 cell parameters used were calculated by the software, including; apical surface area, cell
727 elongation magnitude and orientation, number of junctions per cell, and signal intensities
728 along junctions. In brief, cell surface elongation is characterized by an axis and
729 magnitude, and can be represented by a symmetric tensor at the centroid of a cell (images
730 with red nematic bars). Calculation integrates cell area and shape so that cells of similar
731 shape with different sizes are assigned the same value of cell elongation (see Aigouy et
732 al. 2016 for details equations (Aigouy et al., 2016)).
733
734 Color-code representations of apical surface area, surface elongation, and junction
735 number were generated in Tissue Analyzer. Surface elongation index (magnitude)
736 calculated by the software, was represented as an index from 0 (round) to 1 (line). Surface
737 elongation and planar polarity of proteins were characterized by an axis and magnitude,
738 represented by a symmetric tensor at the centroid of a cell (images with red nematic bars).
739
740 Intensity measurements of immunostaining are presented for every data as the mean
741 intensity along single junctions and normalized to the global mean junctional intensity of
742 corresponding embryos. Anisotropy parameters were calculated from junctional
743 intensities measured within Tissue Analyzer. Intensities were measured along 3 pixel-

744 wide lines (~500nm), measurements were extracted from a database created by the
745 software and used externally for calculations. For each single cell analyzed, the mean
746 junction intensity was used to calculate per cell, the standard deviation between the
747 intensity of all junctions, and the junction with the maximal intensity divided by the junction
748 with the minimal intensity (Max/Min ratio). These two parameters were used to evaluate
749 the anisotropic accumulation of proteins at apical junctions. Double immunostainings
750 were used to assess correlative accumulation of proteins, and mean junction intensities
751 were used to create scatter plots to evaluate the dispersion of the intensity across the
752 populations, and their correlation coefficients. Generally, measurements taken of
753 junctions from different embryos were pooled, except for a few examples in which
754 junctions were grouped by individual cells to evaluate the range of anisotropy in different
755 cells.
756
757 For planar polarity of protein localization at apical junctions, Tissue Analyzer calculates a
758 planar polarity characterized by an axis and magnitude, and can be represented by a
759 symmetric tensor at the centroid of a cell (images with red nematic bars). Cell junctions
760 fluorescent intensity as well as the angles of junction and the geometry of the cell were
761 used to define the magnitude of polarity as well as the angle (see Aigouy et al. 2016 for
762 details equations (Aigouy et al., 2016)). For protein accumulation based on junctional
763 orientation, average junctional intensities were plotted according to junctional orientation
764 angles which were classified in bins of 15°.
765
766 For protein quantifications in *Crb2*$^{-/-}$ mutants and comparison with wild-type (WT)
767 embryos, 3-4 embryos of each genotype recovered from 2-3 litters where processed,
768 immunostained and imaged in parallel using the same parameters, then segmented and
769 quantified as described above. Measurements are presented as the mean intensity along
770 single junctions and normalized to the global mean junctional intensity of the pool cohort
771 of embryos of both genotypes for each proteins. For F-Actin quantification, junctional
772 values represent the intensity measured at the peripheral cortex and the medial values
773 the intensity measured in the medial/cytoplasmic area of the same cells.
774

775 **Time-lapse imaging**

776 For time lapse imaging, mid- to late-streak stage embryos (E7.5) were dissected with their
777 yolk sac and ectoplacental cone intact in dissection medium (CO_2 independent DMEM,
778 10%FBS) at 37°C. Embryos were stabilized in a depression created in a layer of collagen
779 matrix and imaged in glass-bottom 35mm MatTek dishes. They were placed with their
780 posterior side facing the objective and culture in 50% rat serum/50% DMEM media in an
781 incubation chamber at 37°C and 5% CO_2. Embryos were imaged for a total of 3-6h with
782 Z-stacks of 1µm step acquired every 5min (minimum time-scale possible to keep embryo
783 and fluorescent signal integrity) on a Leica-SP8 laser point scanning confocal or a Nikon
784 A1RHD25 high speed resonant scanning confocal with 40x objectives. Imaging usually
785 focused on regions of interest in the proximo-distal middle of the primitive steak where
786 the epiblast is the least curved and optimal for image data acquisition and analysis.

787

788 **Dynamic images analysis and quantification**

789 Membrane-GFP from *mT/mG* embryos was used to observed apical constriction
790 associated with cell ingression at the primitive streak. For all other imaging and
791 quantification, a ZO-1-GFP Knock-in reporter was used as it generally gave the best
792 signal-to-noise enabling observation of apical surfaces of epiblast cells. Analyses were
793 performed in ImageJ and Tissue Analyzer on maximal projections of Z-stacks. Cell
794 tracking in the plane of the epithelium was performed manually using the Manual Tracking
795 plugin in ImageJ. To quantify ingression events, small areas of interest in the vicinity of
796 the primitive streak, corresponding to a ~40µm region along the predicted midline, were
797 analyzed. All cells were tracked for at least one hour, and constriction and ingression
798 events were identified to calculate the ratio of ingression events per hour. Ingression
799 events were considered isolated when the constriction and disappearance of a cell
800 occurred within 30min or more of the ingression of adjacent neighboring cells, and
801 clustered when occurring within a 30min window of the ingression of adjacent neighboring
802 cells (2-4 cells in different clustered events).

803

804 For dynamic analysis of apical surfaces, small regions of interest at the primitive streak
805 were used for segmentation with Tissue analyzer. A first segmentation was automatically

806 generated by the software, then each time-point manually corrected. Cell parameters,
807 including apical surface area, surface elongation index and orientation and number of
808 edges, were extracted from the segmentation database, and graphs were plotted using
809 GraphPad Prism.
810
811 The beginning of cell constriction associated with an ingression event was defined as the
812 point when cells started to reduce their apical surface area after a period of oscillation,
813 and so continually until they completely lost their apical domain. The start of constriction
814 was defined as t0 when the apical surface area, rate of change of surface area and other
815 parameters were plotted against time. Changes in apical surface area (constriction rate)
816 was defined as the inverse value of the derivative of apical surface area: Δarea(t)=area(t-
817 1) – area(t). Oscillations of surface area in epiblast cells away from the primitive streak,
818 and before the initiation of ingression were compared with the more dramatic changes in
819 surface area during the constriction period. During ingression, a constriction pulse was
820 defined as an event in which the contraction rate exceeded one standard deviation above
821 the mean of the contraction rate of non-ingressing cells (above 0.7 μm^2/min). The number
822 of pulses, occurrence of pulse and pulse magnitude were quantified manually for each
823 constriction period of each cell and each pulse. The calculated apical area rate of change
824 was integrated in the Tissue Analyzer database, and used to generate color-coded movie
825 representations of surface area, area rate of changes, cell elongation, number of junctions
826 and junction length. As for fixed embryo analysis, surface elongation index (magnitude)
827 calculated by the software, is represented as an index from 0 (round) to 1 (line). Surface
828 elongation is characterized by an axis and magnitude, and is represented by a symmetric
829 tensor at the centroid of a cell (red nematic bars).
830
831 Changes in junction length (shrinkage rate) was defined similarly to cell area changes, as
832 the inverse value of the derivative of junction length: Δlength(t)=length(t-1) – length(t). To
833 analyze and compare junctions length changes over time, correlation of pairs of junctions
834 were quantified and plot as correlation matrix to illustrate a single cell or correlation
835 coefficient plot for pool of single cells. The average shrinkage rate of single junctions

836 during consecutive cell constriction pulses and stable phases were calculated to visualize
837 the asynchronous and differential shrinkage of junctions during single cell constriction.
838
839 **Statistics**
840 A range of 3 to 6 embryos were analyzed for each experiment. Details of n values, means
841 and p values can be found in Supplementary file 1. Error bars on graphs represent s.e.m.
842 P values corresponds to an unpaired non-parametric Mann-Whitney test for comparison
843 of pairs of conditions, or one-way ANOVA for multiple comparisons. All cells were
844 included in the statistical analysis. Each embryo was considered a biological replicate.
845 No randomisation or blind analysis were conducted.
846
847 **Definition of terms**
848 Start of constriction: the beginning of cell constriction associated with an ingression event
849 at the primitive streak was defined as the time point when cells started to reduce their
850 apical surface area after a period of oscillation, and so continually until they completely
851 lost their apical domain.
852 End of constriction: the end of constriction was defined as the time point when the
853 constricting cells lost their apical surface and move out of the plan of the epiblast.
854 Before constriction: defines the time period before cells start their constriction at the
855 primitive streak. This time-period shows same oscillation characteristics of the apical
856 surface area as epiblast cells further away from the primitive streak.
857 Constriction: defines the time-period during which cells reduced their apical surface area
858 until they completely lose their apical domain. We also use the term for the constriction
859 rate and constriction pulse.
860 Contraction/expansion: used to define the rate of change in apical surface area through
861 time, contraction defining the rate of reduction in area, and expansion a rate of increase
862 in area. They are defined both as positive value and plotted as rate of change, or in some
863 cases defined negatively and positively and plotted as constriction rate.
864 Constriction pulse: defines the time-period during the constriction when the rate of
865 contraction of the apical surface area exceeds the threshold.

866 Stable phases: defines the time-period between constriction pulses, when the change in
867 apical surface area shows minimal variation.
868 Pulse occurrence: defines the frequency at which constriction pulses are occurring.
869 Pulse magnitude: defines as the maximum value of constriction rate within each pulse.
870 Shrinkage: defines the junction reduction in length, Shrinkage rate indicates the change
871 in junction length through time.
872
873
874 **Acknowledgements**

875 AF and AKH dedicate this manuscript to the memory of our late colleague and mentor
876 Kathryn V Anderson. Kathryn marveled at the spectacle of mammalian gastrulation and
877 recognized the insights that genetics and imaging would bring. We thank Andre Le Bivic
878 for the PatJ antibody, Danelle Devenport for the Celsr1 antibody, Jane McGlade for the
879 Crumbs2 antibody and Masatoshi Takeichi for the Rock1 antibody. We thank Terry
880 Lechler for the ZO-1-GFP animals. We thank Zhirong Bao, Alex Joyner, Jen Zallen and
881 members of the Hadjantonakis lab for stimulating discussions and critical feedback on the
882 work. We thank the MSKCC (Memorial Sloan Kettering Cancer Center) Molecular
883 Cytology, and the SKI Light Microscopy Instrument Cluster and James Muller for imaging
884 technical support. This study was supported by the NIH (R01HD094868, R01DK127821,
885 R01HD086478, and P30CA008748). AF was supported by a postdoctoral fellowship from
886 the MSKCC GMTEC (The Alan and Sandra Gerry Metastasis and Tumor Ecosystems
887 Center) for part of this work.

888 Aigouy, B., R. Farhadifar, D.B. Staple, A. Sagner, J.C. Roper, F. Julicher, and S. Eaton. 2010. Cell
889 flow reorients the axis of planar polarity in the wing epithelium of Drosophila. *Cell*.
890 142:773-786.

891 Aigouy, B., D. Umetsu, and S. Eaton. 2016. Segmentation and Quantitative Analysis of Epithelial
892 Tissues. *Methods Mol Biol*. 1478:227-239.

893 Alves, C.H., A.S. Sanz, B. Park, L.P. Pellissier, N. Tanimoto, S.C. Beck, G. Huber, M. Murtaza, F.
894 Richard, I. Sridevi Gurubaran, M. Garcia Garrido, C.N. Levelt, P. Rashbass, A. Le Bivic, M.W.
895 Seeliger, and J. Wijnholds. 2013. Loss of CRB2 in the mouse retina mimics human retinitis
896 pigmentosa due to mutations in the CRB1 gene. *Hum Mol Genet*. 22:35-50.

897 An, Y., G. Xue, Y. Shaobo, D. Mingxi, X. Zhou, W. Yu, T. Ishibashi, L. Zhang, and Y. Yan. 2017. Apical
898 constriction is driven by a pulsatile apical myosin network in delaminating Drosophila
899 neuroblasts. *Development*. 144:2153-2164.

900 Biehler, C., K.E. Rothenberg, A. Jette, H.M. Gaude, R. Fernandez-Gonzalez, and P. Laprise. 2021.
901 Pak1 and PP2A antagonize aPKC function to support cortical tension induced by the
902 Crumbs-Yurt complex. *Elife*. 10.

903 Christodoulou, N., and P.A. Skourides. 2015. Cell-Autonomous Ca(2+) Flashes Elicit Pulsed
904 Contractions of an Apical Actin Network to Drive Apical Constriction during Neural Tube
905 Closure. *Cell Rep*. 13:2189-2202.

906 Chuai, M., W. Zeng, X. Yang, V. Boychenko, J.A. Glazier, and C.J. Weijer. 2006. Cell movement
907 during chick primitive streak formation. *Dev Biol*. 296:137-149.

908 Chung, S., S. Kim, and D.J. Andrew. 2017. Uncoupling apical constriction from tissue invagination.
909 *Elife*. 6.

910 Coravos, J.S., and A.C. Martin. 2016. Apical Sarcomere-like Actomyosin Contracts Nonmuscle
911 Drosophila Epithelial Cells. *Dev Cell*. 39:346-358.

912 Coravos, J.S., F.M. Mason, and A.C. Martin. 2017. Actomyosin Pulsing in Tissue Integrity
913 Maintenance during Morphogenesis. *Trends Cell Biol*. 27:276-283.

914 Curtin, J.A., E. Quint, V. Tsipouri, R.M. Arkell, B. Cattanach, A.J. Copp, D.J. Henderson, N. Spurr, P.
915 Stanier, E.M. Fisher, P.M. Nolan, K.P. Steel, S.D. Brown, I.C. Gray, and J.N. Murdoch. 2003.
916 Mutation of Celsr1 disrupts planar polarity of inner ear hair cells and causes severe neural
917 tube defects in the mouse. *Curr Biol*. 13:1129-1133.

918 Ferrer-Vaquer, A., M. Viotti, and A.K. Hadjantonakis. 2010. Transitions between epithelial and
919 mesenchymal states and the morphogenesis of the early mouse embryo. *Cell Adh Migr*.
920 4:447-457.

921 Foote, H.P., K.D. Sumigray, and T. Lechler. 2013. FRAP analysis reveals stabilization of adhesion
922 structures in the epidermis compared to cultured keratinocytes. *PLoS One*. 8:e71491.

923 Francou, A., and K.V. Anderson. 2020. The Epithelial-to-Mesenchymal Transition (EMT) in
924 Development and Cancer. *Annu Rev Cancer Biol*. 4:197-220.

925 Hayashi, S., P. Lewis, L. Pevny, and A.P. McMahon. 2002. Efficient gene modulation in mouse
926 epiblast using a Sox2Cre transgenic mouse strain. *Mech Dev*. 119 Suppl 1:S97-S101.

927 Heer, N.C., and A.C. Martin. 2017. Tension, contraction and tissue morphogenesis. *Development*.
928 144:4249-4260.

929 Huebner, R.J., T. Lechler, and A.J. Ewald. 2014. Developmental stratification of the mammary
930 epithelium occurs through symmetry-breaking vertical divisions of apically positioned
931 luminal cells. *Development*. 141:1085-1094.

932 Ishiuchi, T., and M. Takeichi. 2011. Willin and Par3 cooperatively regulate epithelial apical
933 constriction through aPKC-mediated ROCK phosphorylation. *Nat Cell Biol*. 13:860-866.

934 Lecuit, T., and P.F. Lenne. 2007. Cell surface mechanics and the control of cell shape, tissue
935 patterns and morphogenesis. *Nat Rev Mol Cell Biol*. 8:633-644.

936 Lim, J., and J.P. Thiery. 2012. Epithelial-mesenchymal transitions: insights from development.
937 *Development*. 139:3471-3486.

938 Mahaffey, J.P., J. Grego-Bessa, K.F. Liem, Jr., and K.V. Anderson. 2013. Cofilin and Vangl2
939 cooperate in the initiation of planar cell polarity in the mouse embryo. *Development*.
940 140:1262-1271.

941 Marston, D.J., C.D. Higgins, K.A. Peters, T.D. Cupp, D.J. Dickinson, A.M. Pani, R.P. Moore, A.H. Cox,
942 D.P. Kiehart, and B. Goldstein. 2016. MRCK-1 Drives Apical Constriction in C. elegans by
943 Linking Developmental Patterning to Force Generation. *Curr Biol*. 26:2079-2089.

944 Martin, A.C., and B. Goldstein. 2014. Apical constriction: themes and variations on a cellular
945 mechanism driving morphogenesis. *Development*. 141:1987-1998.

946 Martin, A.C., M. Kaschube, and E.F. Wieschaus. 2009. Pulsed contractions of an actin-myosin
947 network drive apical constriction. *Nature*. 457:495-499.

948 Mason, F.M., M. Tworoger, and A.C. Martin. 2013. Apical domain polarization localizes actin-
949 myosin activity to drive ratchet-like apical constriction. *Nat Cell Biol*. 15:926-936.

950 Mathiah, N., E. Despin-Guitard, M. Stower, W. Nahaboo, E.S. Eski, S.P. Singh, S. Srinivas, and I.
951 Migeotte. 2020. Asymmetry in the frequency and position of mitosis in the mouse embryo
952 epiblast at gastrulation. *EMBO Rep*. 21:e50944.

953 McDole, K., L. Guignard, F. Amat, A. Berger, G. Malandain, L.A. Royer, S.C. Turaga, K. Branson,
954 and P.J. Keller. 2018. In Toto Imaging and Reconstruction of Post-Implantation Mouse
955 Development at the Single-Cell Level. *Cell*. 175:859-876 e833.

956 Morgani, S.M., and A.K. Hadjantonakis. 2020. Signaling regulation during gastrulation: Insights
957 from mouse embryos and in vitro systems. *Curr Top Dev Biol*. 137:391-431.

958 Muzumdar, M.D., B. Tasic, K. Miyamichi, L. Li, and L. Luo. 2007. A global double-fluorescent Cre
959 reporter mouse. *Genesis*. 45:593-605.

960 Nakaya, Y., and G. Sheng. 2008. Epithelial to mesenchymal transition during gastrulation: an
961 embryological view. *Dev Growth Differ*. 50:755-766.

962 Nishimura, T., H. Honda, and M. Takeichi. 2012. Planar cell polarity links axes of spatial dynamics
963 in neural-tube closure. *Cell*. 149:1084-1097.

964 Petrov, D., I. Dahan, E. Cohen-Kfir, and S. Ravid. 2017. aPKCzeta affects directed cell migration
965 through the regulation of myosin light chain phosphorylation. *Cell Adh Migr*. 11:347-359.

966 Ramkumar, N., and K.V. Anderson. 2011. SnapShot: mouse primitive streak. *Cell*. 146:488-488
967 e482.

968 Ramkumar, N., T. Omelchenko, N.F. Silva-Gagliardi, C.J. McGlade, J. Wijnholds, and K.V.
969 Anderson. 2016. Crumbs2 promotes cell ingression during the epithelial-to-mesenchymal
970 transition at gastrulation. *Nat Cell Biol*. 18:1281-1291.

971 Roh-Johnson, M., G. Shemer, C.D. Higgins, J.H. McClellan, A.D. Werts, U.S. Tulu, L. Gao, E. Betzig,
972 D.P. Kiehart, and B. Goldstein. 2012. Triggering a cell shape change by exploiting
973 preexisting actomyosin contractions. *Science*. 335:1232-1235.

974 Roper, K. 2012. Anisotropy of Crumbs and aPKC drives myosin cable assembly during tube
975 formation. *Dev Cell*. 23:939-953.

976 Rozbicki, E., M. Chuai, A.I. Karjalainen, F. Song, H.M. Sang, R. Martin, H.J. Knolker, M.P.
977 MacDonald, and C.J. Weijer. 2015. Myosin-II-mediated cell shape changes and cell
978 intercalation contribute to primitive streak formation. *Nat Cell Biol*. 17:397-408.

979 Samarage, C.R., M.D. White, Y.D. Alvarez, J.C. Fierro-Gonzalez, Y. Henon, E.C. Jesudason, S.
980 Bissiere, A. Fouras, and N. Plachta. 2015. Cortical Tension Allocates the First Inner Cells of
981 the Mammalian Embryo. *Dev Cell*. 34:435-447.

982 Serrano Najera, G., and C.J. Weijer. 2020. Cellular processes driving gastrulation in the avian
983 embryo. *Mech Dev*. 163:103624.

984 Sidor, C., T.J. Stevens, L. Jin, J. Boulanger, and K. Roper. 2020. Rho-Kinase Planar Polarization at
985 Tissue Boundaries Depends on Phospho-regulation of Membrane Residence Time. *Dev*
986 *Cell*. 52:364-378 e367.

987 Simoes, S., G. Lerchbaumer, M. Pellikka, P. Giannatou, T. Lam, D. Kim, J. Yu, D. Ter Stal, K. Al
988 Kakouni, R. Fernandez-Gonzalez, and U. Tepass. 2022. Crumbs complex-directed apical
989 membrane dynamics in epithelial cell ingression. *J Cell Biol*. 221.

990 Simoes, S., Y. Oh, M.F.Z. Wang, R. Fernandez-Gonzalez, and U. Tepass. 2017. Myosin II promotes
991 the anisotropic loss of the apical domain during Drosophila neuroblast ingression. *J Cell*
992 *Biol*. 216:1387-1404.

993 Thiery, J.P. 2002. Epithelial-mesenchymal transitions in tumour progression. *Nat Rev Cancer*.
994 2:442-454.

995 Thiery, J.P., H. Acloque, R.Y. Huang, and M.A. Nieto. 2009. Epithelial-mesenchymal transitions in
996 development and disease. *Cell*. 139:871-890.

997 Voiculescu, O., F. Bertocchini, L. Wolpert, R.E. Keller, and C.D. Stern. 2007. The amniote primitive
998 streak is defined by epithelial cell intercalation before gastrulation. *Nature*. 449:1049-
999 1052.

1000 Voiculescu, O., L. Bodenstein, I.J. Lau, and C.D. Stern. 2014. Local cell interactions and self-
1001 amplifying individual cell ingression drive amniote gastrulation. *Elife*. 3:e01817.

1002 Williams, M., C. Burdsal, A. Periasamy, M. Lewandoski, and A. Sutherland. 2012. Mouse primitive
1003 streak forms in situ by initiation of epithelial to mesenchymal transition without migration
1004 of a cell population. *Dev Dyn*. 241:270-283.

1005 Ye, X., and R.A. Weinberg. 2015. Epithelial-Mesenchymal Plasticity: A Central Regulator of Cancer
1006 Progression. *Trends Cell Biol*. 25:675-686.
1007

1008

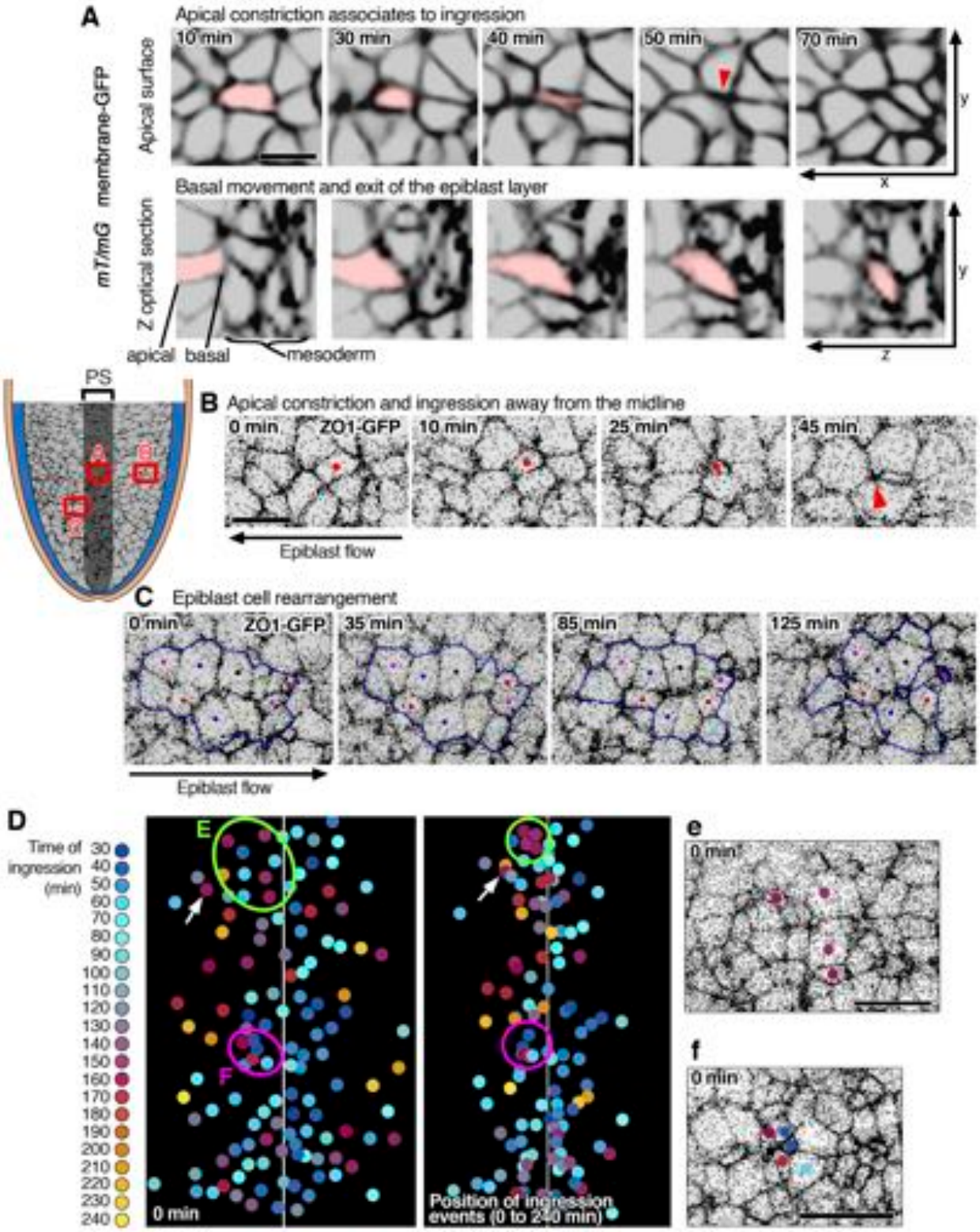

Figure 1-figure supplement 1: Apical constriction and ingression of epiblast cells in the vicinity of the mouse primitive streak. **(A)** Snapshots of a time-lapse of membrane-GFP in an *mTmG* embryo showing apical surface constriction in a single Z plan below the apical membrane (top

1013 row) associated to ingression out of the epiblast layer and integration to the mesoderm seen on
1014 apicobasal Z optical section (bottom row) at the primitive streak (region located on the
1015 schematic). **(B)** Example of cell constricting away from the midline, as the epiblast cells move
1016 toward the primitive streak. **(C)** Example showing cell rearrangement among a cluster of
1017 epiblast cells near the primitive streak. **(D)** Color-coded time-series and position of ingression
1018 events of tracked cells shown in Figure 1d,e. The initial position of a circled group of cells (green
1019 circle) is shown in e; cells are not all neighbors at 0min but ingress together as neighbors (after
1020 165min). Another group of cells (purple circle) who's initial position is shown in f; cells are
1021 neighbors at 0min, but they do not ingress at the same time. Cells are considered to constrict
1022 and ingress as isolated cells when their ingression takes place 30min or more from their
1023 neighbors. White arrow shows the ingression of an isolated cell.
1024 Scale bars A,B,C 10μm; E,F 20μm.
1025
1026

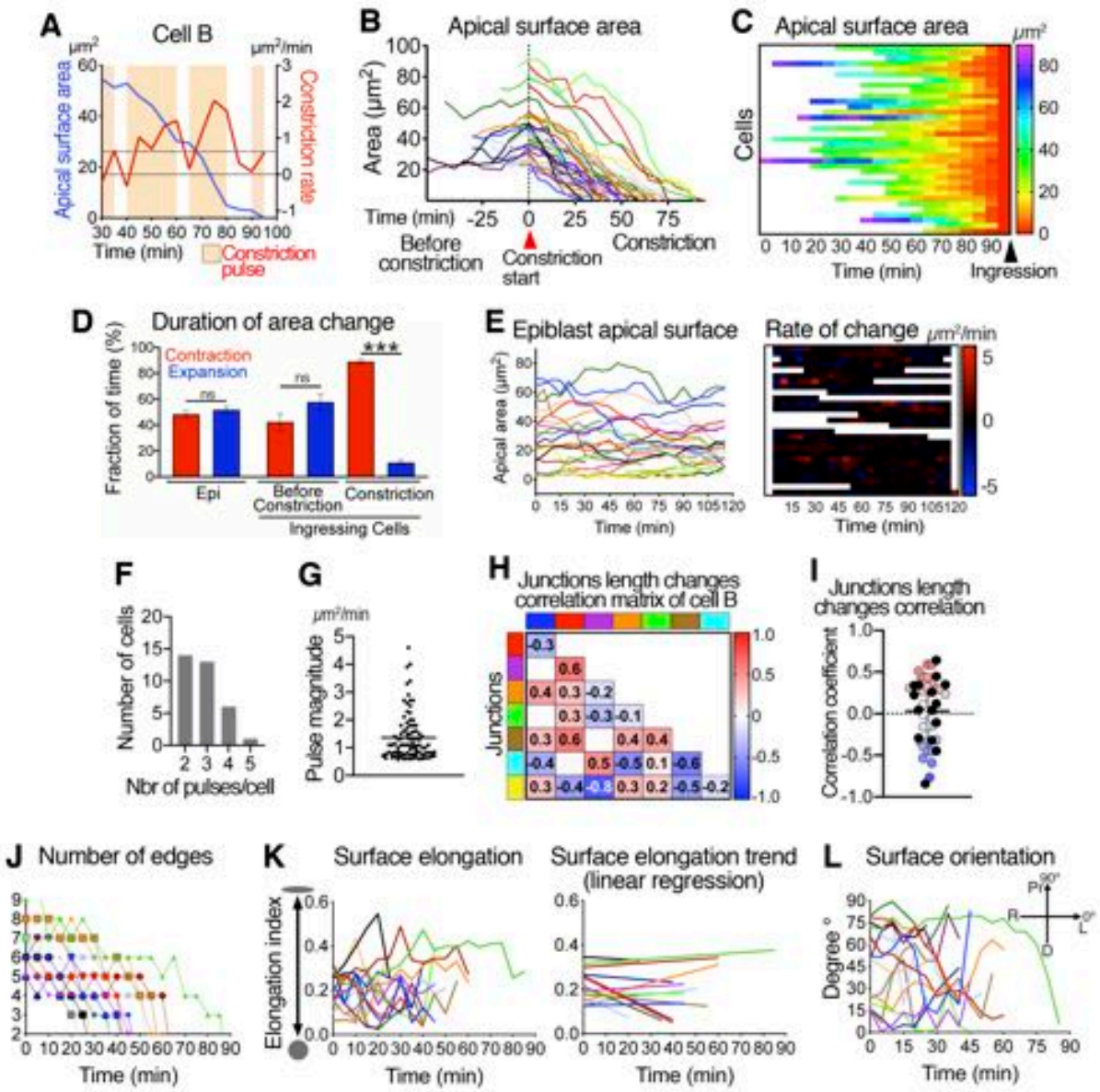

Figure 2,3-figure supplement 1: Details and features of constriction pulses and cell parameters during constriction. **(A)** Graph of apical surface area and rate of constriction of single cell B (shown in Figure 3D,E) exhibiting four pulses of constriction (beige regions). **(B)** Plot showing the apical surface area of several cells at the primitive streak during the total time of the analysis. 0min marks the beginning of the constriction period. Cells begin with a wide range of different initial apical surfaces prior to their constriction. **(C)** Heat map plot of the apical surface area during constriction showing the reduction in area and the pulses of constriction. Each row represents data for an individual cell. **(D)** Fraction of time cells spend contracting or expending their apical surfaces revealing equilibrium in lateral epiblast and at the streak before the constriction period, followed by significantly longer contraction time during constriction. **(E)**

1038 Plot showing the apical surface area and heat map color-code of rate of change of epiblast cells
1039 outside the region occupied by the primitive streak before ingression. Cells exhibit a wide variety
1040 of apical areas, and fluctuate their apical surfaces, with a low rate of contraction and expansion
1041 through time. (Corresponding measurements are shown in D and Figure 2E). **(F)** Frequency
1042 distribution graph showing the proportion of cells undergoing two to four main constriction
1043 pulses. **(G)** Dot plot showing the average magnitude of constriction pulses. **(H)** Matrix heat map
1044 showing the correlation of junction length changes through time of cell B shown in a and 2i,j.
1045 Some junctions show correlation and change their length during the same time when others
1046 show anti-correlation. Each row and column represent a single junction and are color-coded as
1047 in a and 2I,J. Numbers represent the correlation coefficients of each pairs of junction compared.
1048 **(I)** Dot plot showing the correlation coefficients of junction length changes through time of
1049 junctions from multiple cells. Correlation of junctions shown in H are colored. **(J)** Plot showing
1050 the number of edges during the constriction period. Cells have different initial numbers of edges,
1051 and gradually lose them during the constriction period. **(K)** Plot showing the apical surface
1052 elongation index calculated by Tissue Analyzer, from 0 to 1, with 0 being perfectly round, and 1
1053 corresponding to a line. Cells show fluctuation in their elongation during constriction, but exhibit
1054 no significant trend (trend showed by the linear regressions). **(L)** Plot showing apical surface
1055 orientation in the plane of the epiblast epithelial layer. Cells show fluctuation of orientation axis
1056 during constriction, and do not show significant pattern of elongation.
1057 41 cells quantified from 4 embryos. *$P<0.05$ (Unpaired bilateral Mann-Whitney test). Error bars
1058 represent s.e.m. Scale bar, 10μm
1059
1060

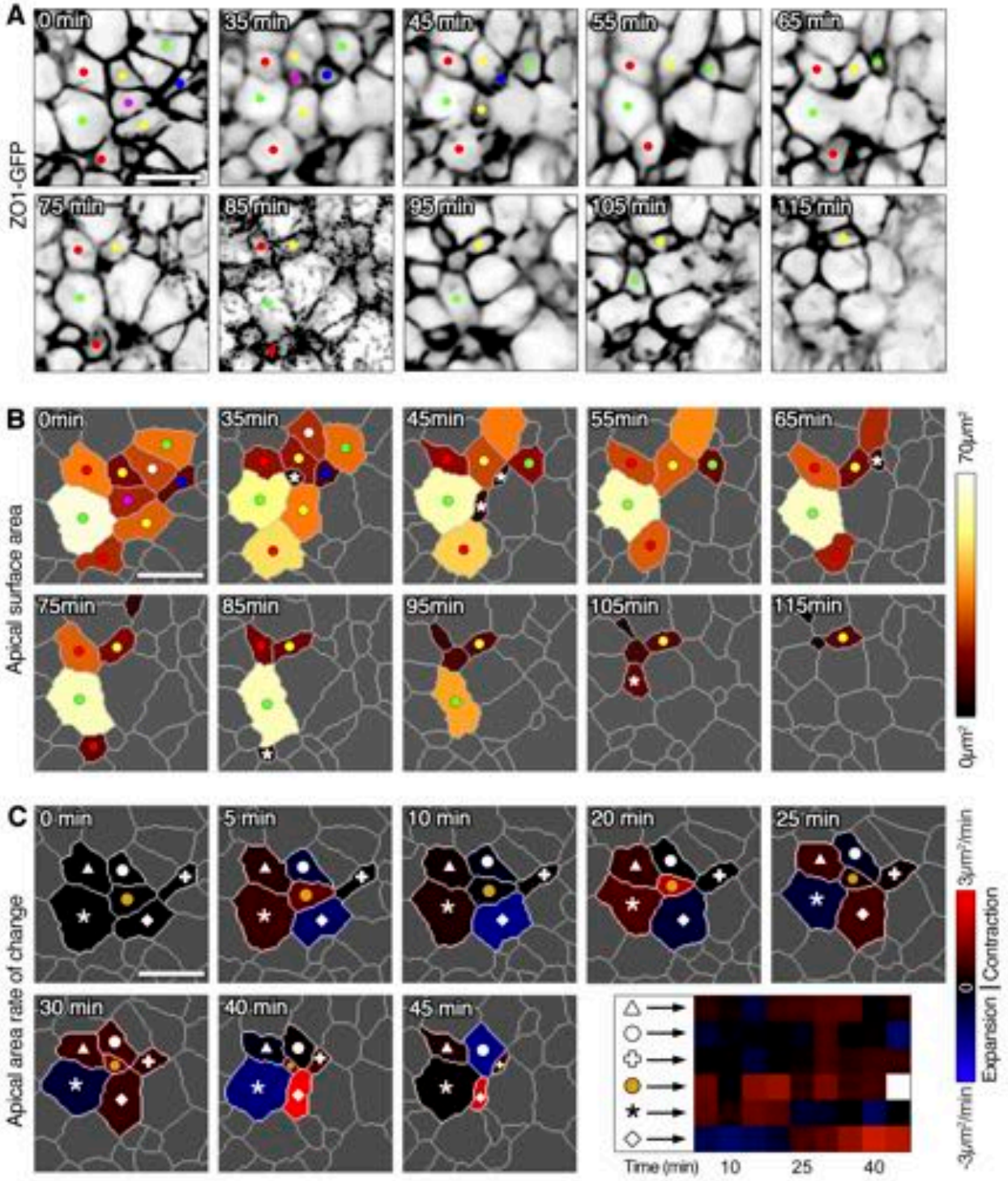

Figure 2-figure supplement 2: Asynchronous apical constriction at the multi-cellular level. **(A)** Time-series of ZO-1-GFP reporter expression identifying a cluster of epiblast cells exhibiting apparent stochastic apical constriction and cell ingression. **(B)** Membrane segmentation and color-coded time-series of apical surface area showing oscillation in apical surfaces in the cell

1066 cluster and asynchronous reduction of apical surfaces during ingression (asterisks). **(C)** Color-
1067 coded time-series and heat map plot of rate of change of apical surface area showing
1068 asynchronous oscillation in area and asynchronous constriction. Note that as one cell in the
1069 middle constricts and ingresses (orange dot), neighboring cells asynchronously change their
1070 apical surfaces; some will constrict and ingress shortly after, while others will only ingress at a
1071 later time point. Each row represents data for an individual cell. Scale bars, 10μm
1072

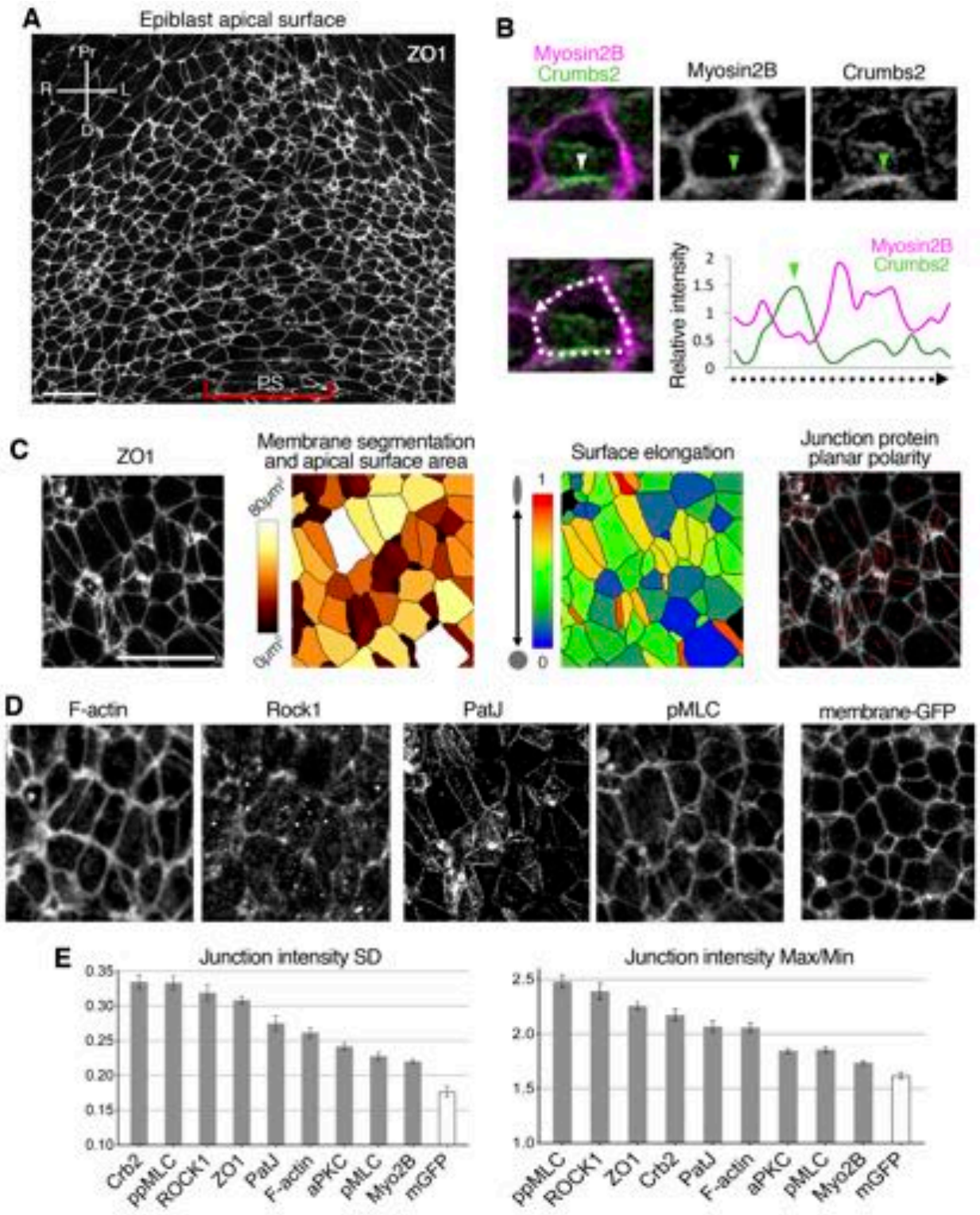

Figure 4-figure supplement 1: Complementary accumulation of Crumbs2 and Myosin2B, and anisotropy of apical components at the primitive streak. **(A)** ZO-1 immunostaining on fixed E7.5 embryo showing the apical surface of epiblast cells in the posterior. **(B)** High magnification view

1077 of a single cell stained for Myosin2B (magenta) and Crumbs2 (green) showing strong Crumbs2
1078 accumulation on one junction (arrowhead) and predominant Myosin accumulation on other
1079 junctions. White dashed line and arrow indicate the membrane intensity measurement shown in
1080 the plot. The junction with the highest level of Crumbs2 (arrowhead) has the lowest level of
1081 Myosin, whereas Myosin predominates (and Crumbs is reduced) at the rest of the junctions. **(C)**
1082 ZO-1 immunostaining used for cell apical membrane identification and segmentation, allows
1083 quantification of junctional intensity of staining, and determination of a number of parameters,
1084 including apical surface area, surface elongation and protein planar polarity. **(D)** Staining F-
1085 actin, Rock1, PatJ and pMLC exhibiting different patterns of accumulation at apical cell-cell
1086 junctions, and a membrane-GFP reporter more homogeneously present at the apical
1087 membrane. **(E)** Plots of anisotropy parameters, junctional Standard Deviation and Max/Min.
1088 Proteins exhibit a range of distributions and anisotropy levels, some like Crumbs2 and ppMLC
1089 show a high level of anisotropy, others like PatJ and F-Actin show moderate anisotropy, and
1090 some like aPKC pMLC and Myosin2B show a lower level of anisotropy closer to the level of the
1091 negative control membrane-GFP. Error bars represent s.e.m.
1092

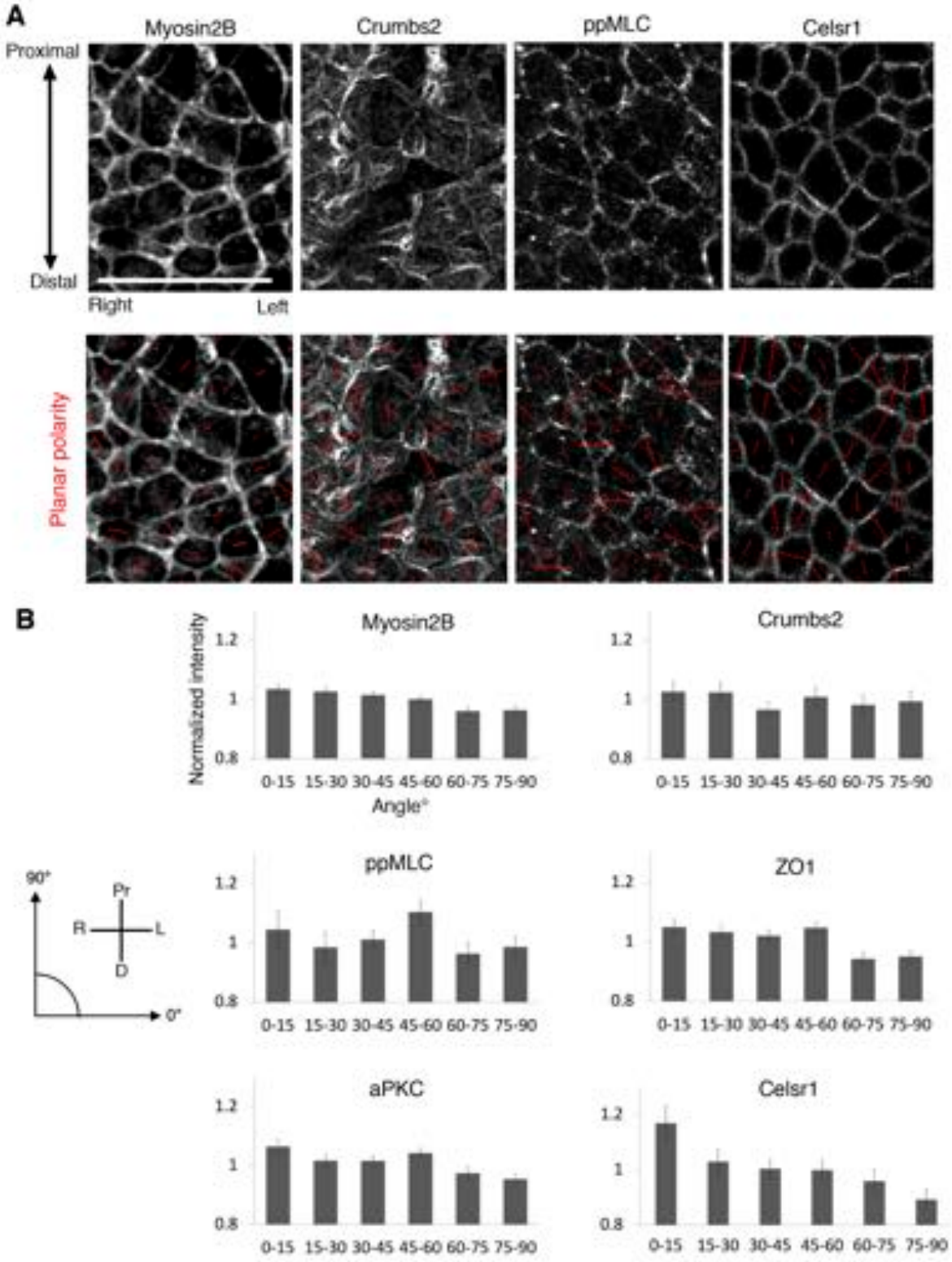

Figure 4-figure supplement 2: Apical proteins show anisotropy accumulation but no planar polarity. **(A)** Immunostaining for Myosin2B, Crumbs2, ppMLC and Celsr1 with associated polarity visualization (red tensor) calculated after membrane segmentation, showing the

1097 orientation (orientation of the tensor) and amplitude of polarity (length of the tensor). **(B)**
1098 Junctional protein intensity plotted as a function of junctional angle. 0° is parallel to the left/right
1099 axis and 90° is parallel to the proximal/distal axis.
1100 The apical proteins described previously and measured here (Myosin2B, Crumbs2, ppMLC, ZO-
1101 1 and aPKC) do not show planar polarity, red bars in A showing polarity of intensity are not
1102 oriented in specific axis, and intensity in B show no bias at a particular angle. By contrast, the
1103 PCP protein Celsr1 exhibits evident polarity, red bars tend to be vertically oriented, and intensity
1104 in B shows a significant increase in Celsr1 levels at edges oriented parallel to the left/right axis.
1105 Celsr1 preferentially accumulates at horizontal junctions (left-right embryo orientation). Error
1106 bars represent s.e.m.
1107

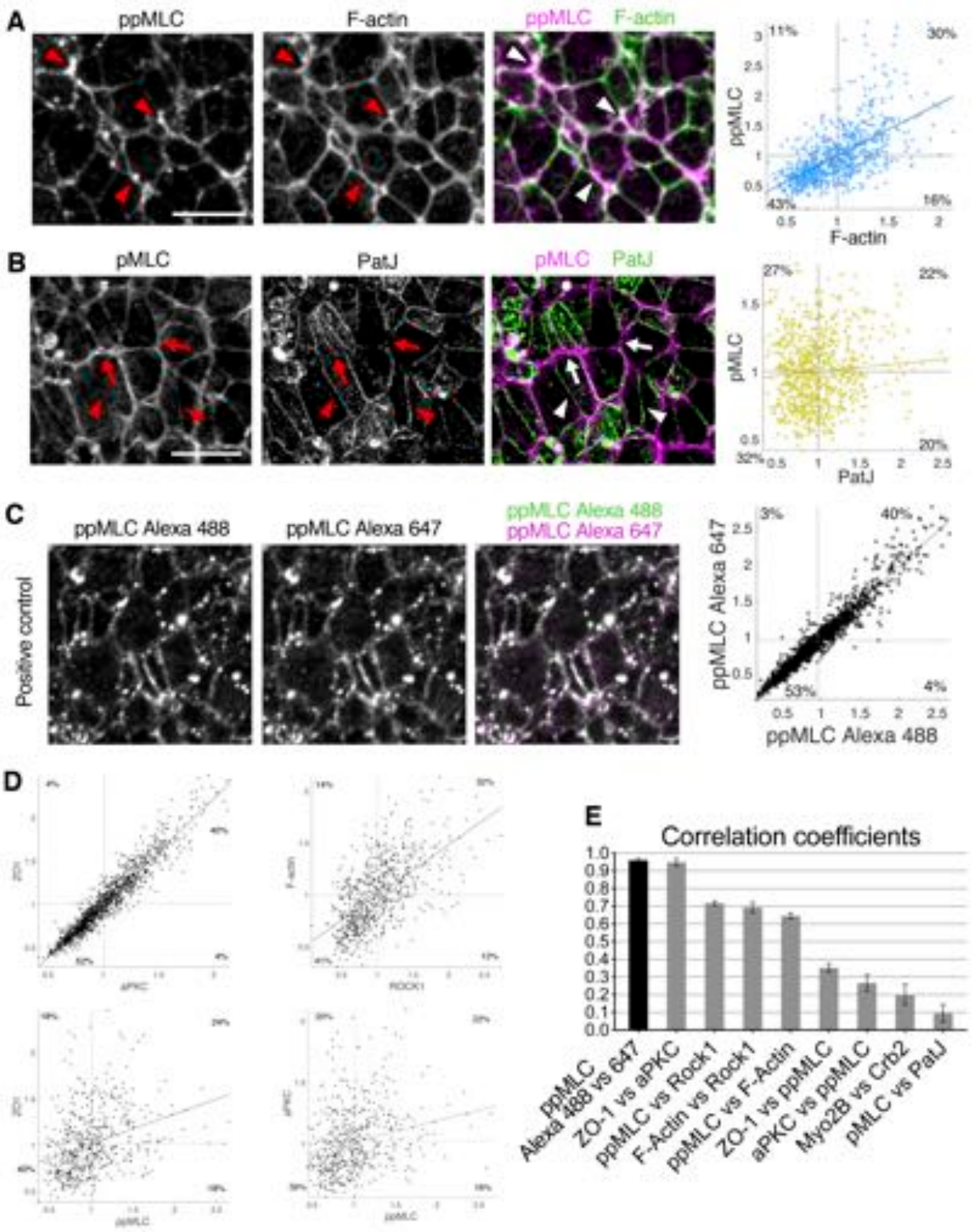

Figure 5-figure supplement 1: Correlation of protein distributions at apical junctions. **(A)** Co-immunostaining of ppMLC and F-Actin reveals a tendency to accumulate on the same junctions. Note colocalization of fluorescent signal on most junctions (arrowheads). Scatter plot on the

1112 right showing elevated intensity correlation of the two proteins. Each point represented the
1113 mean intensity at a single junction. **(B)** Co-immunostaining of pMLC and PatJ reveals that they
1114 tend to accumulate on different junctions. Note junctions where Myosin accumulation
1115 predominates (arrows), and junctions where Crumbs2 predominates (arrowheads).
1116 Corresponding scatter plot shows more spread distribution and no correlation. **(C)**
1117 Immunostaining for ppMLC simultaneously revealed by two distinct secondary antibodies (Alexa
1118 488 and 647) as positive control, and corresponding scatter plot showing strong junctional
1119 intensity correlation after membrane segmentation. **(D)** Scatter plots showing the correlation of
1120 intensity of other pairs of proteins. **(E)** Correlation coefficients associated with scatter plots
1121 shown in A,B,C,D and Figure 5. Error bars represent s.e.m.
1122

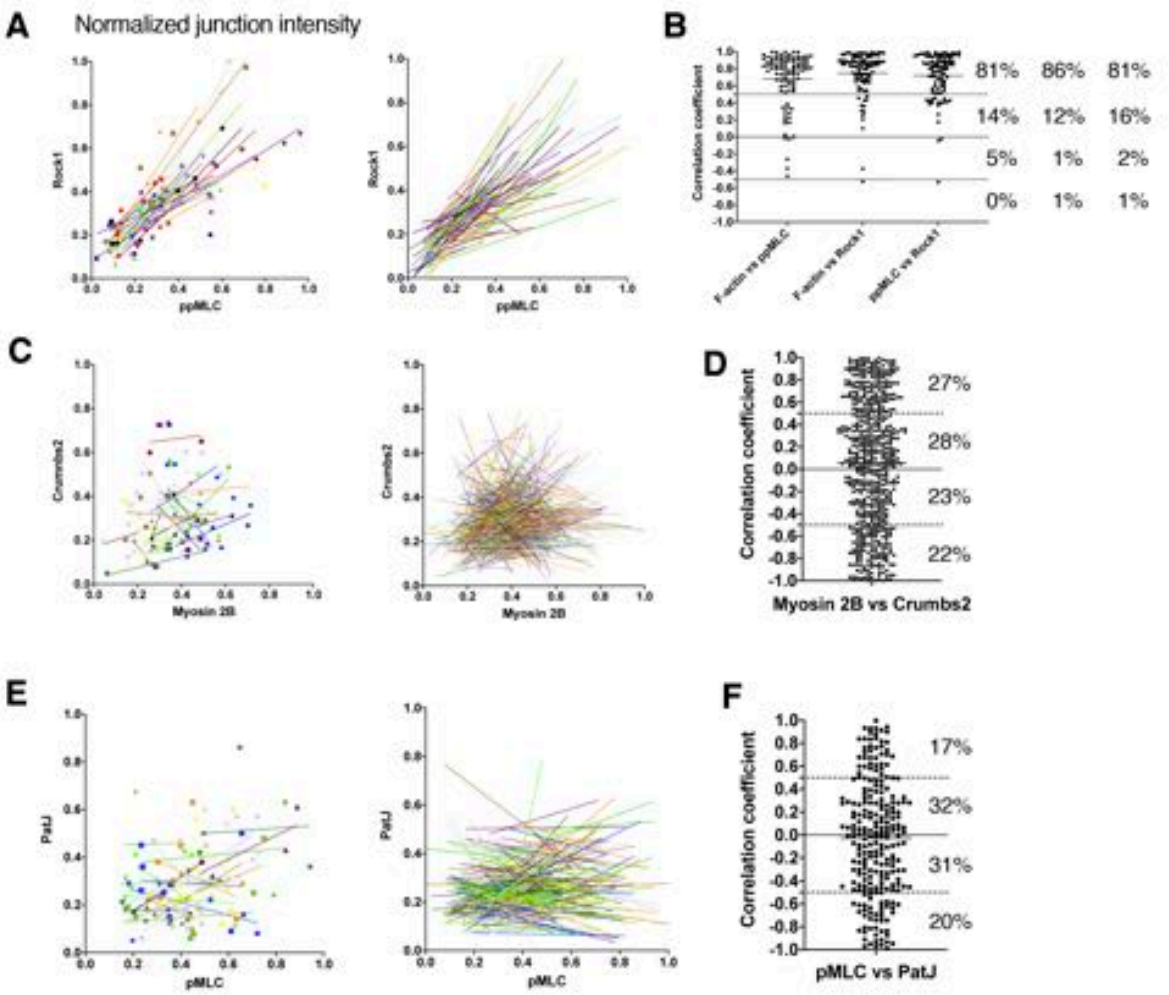

Figure 5-figure supplement 2: Junctional correlation of proteins at the single cell level. **(A)** Example of scatter plot showing the junctional intensity correlation of ppMLC and Rock1 in a cohort of cells. Each symbol represents one junction, grouped by cells (color coded) with respective correlation trends. Plot on the right shows only the correlation trend for a larger number of cells. **(B)** Correlation coefficients of ppMLC and Rock1 from plot shown in A, as well as F-actin and ppMLC, and F-actin and Rock1. Each dot represents the coefficient of correlation of junctions intensity of a single cell. % show the distribution of correlation coefficients in the different quarters. **(C)** Example of junctional intensity correlation of single cells for Crumbs2 and Myosin2B, depicting a mix of cells with correlation, some with no correlation, and some with anti-correlation. **(D)** Correlation coefficients reflecting the scatter plot shown in C, showing a broad distribution, from correlation (+1) to anti-correlation (-1). % show the distribution of correlation coefficients. **(E)** Example of junctional intensity correlation of single cells for PatJ and pMLC, depicting a mix of cells with correlation, some with no correlation, and some with anti-correlation. **(F)** Correlation coefficients reflecting the scatter plot shown in C, showing a broad

distribution, from correlation (+1) to anti-correlation (-1). % show the distribution of correlation coefficients.

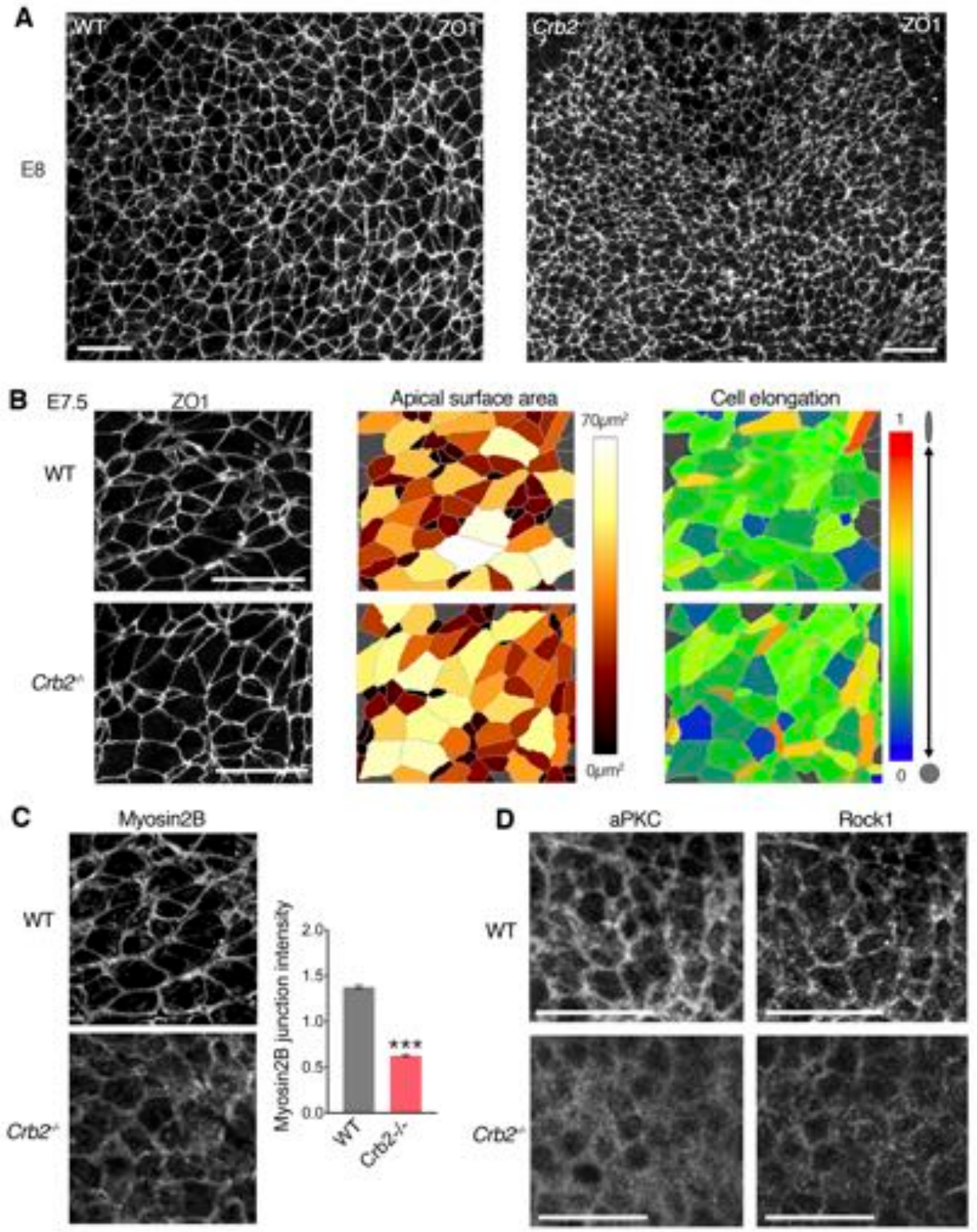

Figure 6,7-figure supplement 1: Cellular and molecular defects in *Crumbs2* mutant embryos. **(A)** Low magnification of ZO-1 staining show in the posterior epiblast in WT and *Crumbs2* mutants at E8.0. **(B)** ZO-1 immunostaining showing the apical surface of WT and *Crumbs2*

1145 mutant embryos at E7.5. Segmentation and color code of apical surface areas and surface
1146 elongation reveal normal size and shape of apical surface area in *Crumbs2* mutants at E7.5. **(C)**
1147 Immunostaining for Myosin2B at E7.5, showing reduced intensity in *Crumbs2* mutant embryos
1148 compared to WT. Graph shows significantly reduced Myosin2B intensity at junctions. **(D)**
1149 Immunostaining for aPKC and Rock1 in WT and *Crumbs2* mutants at E7.5 (intensity
1150 quantifications shown in Figure 7C).
1151 ***P<0.001 (Unpaired bilateral Mann-Whitney test). Error bars represent s.e.m.
1152
1153
1154 **Video S1.** Time-lapse imaging of a membrane-GFP reporter (recombined *mT/mG*)
1155 expressing embryo at embryonic day E7.5, showing apical constriction (right panel)
1156 associated to ingression, as cells move out of the epiblast epithelial layer basally to join
1157 the underlying mesoderm (left panel). Images were denoised and deconvolved, and
1158 represent single planes of optical sections and apical cell surfaces. The time-lapse
1159 spans 70min with 10min interval between frames.
1160
1161 **Video S2**. Time-lapse imaging of the posterior of a ZO-1-GFP reporter expressing
1162 embryo in the vicinity of the primitive streak at embryonic day E7.5. Tracking of
1163 individual cells reveals lateral epiblast cells converging toward the midline prior to their
1164 ingression. Cells around the midline (middle row) do not exhibit extensive movement in
1165 the plane of the epithelium. Movie of 240min with 5min interval between frames.
1166
1167 **Video S3**. Time-lapse of ZO-1-GFP showing rearrangement of cells in the epiblast near
1168 the primitive streak (top panel, 125min), and cell apical constriction and ingression away
1169 from the primitive streak, as the epiblast flows (to the left side) toward the midline
1170 (bottom panel, 55min). 5min interval between frames.
1171
1172 **Video S4**. Time-lapse of ZO-1-GFP highlighting 3 cells apically constricting and
1173 ingressing in the primitive streak region. 60min total with 5min interval between frames.
1174
1175 **Video S5**. Time-lapse of ZO-1-GFP highlighting a single cell at the primitive streak
1176 apically constricting. Membrane segmentation is performed over time such that different

1177 parameters can be followed and quantified, including the apical surface area, a cell's
1178 elongation and orientation, and the number of junctions. 95min total with 5min interval
1179 between frames.
1180
1181 **Video S6**. Segmentation of time-lapse showing color-code of cell apical surface (left
1182 panel), constriction rate (middle panel) and junction length (right panel) of a cell A
1183 shown in Figure 2. 40min total with 5min interval between frames.
1184
1185 **Video S7.** Time-lapse of ZO-1-GFP showing a cell cluster at the primitive streak. Most
1186 of the cells gradually constrict and ingress, and cells tracked after segmentation and
1187 color-coded for apical surface area and changes in surface area. Images were denoised
1188 and deconvolved. 115min with 5min interval between frames.
1189